universität wien

MASTERARBEIT / MASTER'S THESIS

Titel der Masterarbeit / Title of the Master's Thesis

Gravitational contraction and galaxy formation in scalar field dark matter cosmologies

verfasst von / submitted by

Kevin Pils, BSc

angestrebter akademischer Grad / in partial fulfilment of the requirements for the degree of

Master of Science (MSc)

Wien, 2021 / Vienna, 2021

Studienkennzahl lt. Studienblatt / degree programme code as it appears on the student record sheet:	UA 066 861
Studienrichtung lt. Studienblatt / degree programme as it appears on the student record sheet:	Masterstudium Astronomie UG2002
Betreut von / Supervisor:	Mag. Mag. Dr. Tanja Rindler-Daller

Acknowledgements

There are no proper words to convey my gratitude and appreciation for my supervisor Mag. Mag. Dr. Rindler-Daller, whose excellent knowledge of the field and eye for detail enabled me to deliver the best possible thesis I could have hoped for. Thanks to her continuous support and guidance it was a pleasure to invest countless hours into this work. Furthermore, I also want to thank my friends and family for their encouragement during the last five years of studies.

Abstract

Our current understanding of the Universe is based on the assumption that dark matter outweighs baryonic matter by a factor of 5, leading to the development of a multitude of theories to explain this "missing mass". Nowadays, the ΛCDM model has been established as the Standard Model of Cosmology due to its ability to correctly describe the Universe on large scales. Despite its success, backed by observations and simulations, it is unable to accurately describe structure on the scale of dwarf galaxies; these deviations are usually denoted as the small-scale problems. In recent years, scalar field dark matter (SFDM, also Bose-Einstein condensed dark matter (BECDM) or ψDM) has been widely studied as a possible solution of these problems. In this work we investigate the evolution of SFDM halo density and circular velocity profiles through adiabatic contraction (AC), as has been studied before for standard (collisionless) CDM. We provide a thorough calculation for several key quantities based on the foundation of the Gross-Pitaevskii-Poisson equations, followed by calculations of the action integrals in the Quantum-Hamilton-Jacobi framework of such systems. These actions are then solved numerically, to verify the validity of the assumptions going into AC. We test AC for SFDM haloes in the "strongly repulsive" self-interacting limit, known as the Thomas-Fermi regime, with a wide range of core radii, $R_{\mathrm{TF}} = 0.1 - 4$ kpc, typically found in dwarf galaxies. We show that the inclusion of baryons exacerbates the small-scale problems for typical cusp-core haloes of $M_{200} \sim 10^{11} M_{\odot}$ when small core radii are considered. However, kpc-sized cores lead to rotation curves in accordance with observations even when including baryons, which is not the case for CDM or fuzzy dark matter (FDM), the non-interacting limit of SFDM. Considering recent research on the Thomas-Fermi regime that favours sub-kpc cores, our findings may imply severe constraints for the parameter range of core sizes in the SFDM model.

Zusammenfassung

Unser derzeitiges Verständnis des Universums basiert auf der Annahme, dass dunkle Materie die baryonische Materie um einen Faktor 5 überwiegt, was zur Entwicklung einer Vielzahl von Theorien zur Erklärung dieser "fehlenden Masse" führte. Heutzutage hat sich das ΛCDM-Modell aufgrund seiner Fähigkeit, das Universum auf großen Skalen korrekt zu beschreiben, als das Standardmodell der Kosmologie etabliert. Trotz seines Erfolgs, gestützt sowohl durch Beobachtungen als auch Simulationen, ist es nicht in der Lage, die Struktur auf Skalen von Zwerggalaxien genau zu beschreiben; diese Abweichungen werden üblicherweise als "small-scale problems" bezeichnet. Als mögliche Lösung dieser Probleme kam in den letzten Jahren die sogenannte Skalarfeld-Dunkle Materie (SFDM, auch Bose-Einstein-kondensierte Dunkle Materie (BECDM) oder ψDM genannt) immer mehr in den Fokus. In dieser Arbeit untersuchen wir die Entwicklung der SFDM-Halodichte und der dazugehörigen Geschwindigkeitsprofile als Folge der adiabatischen Kontraktion (AC), wie sie zuvor für die im Standardmodell beschriebene (d.h. stoßfreie) dunkle Materie untersucht wurden. Wir bieten eine gründliche Berechnung mehrerer wichtiger physikalischer Größen basierend auf der Grundlage der Gross-Pitaevskii-Poisson-Gleichungen, gefolgt von Berechnungen der Wirkungsintegrale im Rahmen der Quanten-Hamilton-Jacobi-Gleichung solcher Systeme. Diese Wirkungen werden anschließend numerisch gelöst, um die Gültigkeit der Annahmen zu überprüfen, die für adiabatische Kontraktion benötigt werden. Wir testen diese Kontraktion für SFDM-Halos im Thomas-Fermi Regime, in dem es zu "stark abstoßenden" Wechselwirkungen der Teilchen kommt, und für einen großen Bereich von Kernradien, $R_{\rm TF} = 0.1 - 4$ kpc, welche typischerweise in Zwerggalaxien gefunden werden. Wir zeigen, dass die Berücksichtigung von Baryonen die "small-scale problems" für typische "cusp-core"-Halos mit $M_{200} \sim 10^{11} M_\odot$ verschärft, wenn letztere kleine Kernradien aufweisen. Im Gegensatz dazu führen jedoch Halos mit Kernradien im kpc-Bereich zu Rotationskurven die sich mit Beobachtungen decken, selbst wenn Baryonen einbezogen werden. Dies ist weder für das Standardmodell der dunklen Materie, noch for Fuzzy Dark Matter (FDM), dem wechselwirkungsfreien Regime von SFDM, der Fall. In Anbetracht der neuesten Erkenntnisse zum Thomas-Fermi Regime, welche zeigen, dass sub-kpc-Halokerne bevorzugt werden, könnten unsere Ergebnisse schwerwiegende Einschränkungen für den Parameterbereich der Kernradien im SFDM-Modell implizieren.

Contents

Chapter 1

Introduction

Controversial ideas, often in complete contradiction to the knowledge at that time, have repeatedly turned out to be a better fit to observations than foregoing concepts, such as Einstein's theories of special and general relativity (Einstein (1905) and Einstein (1916), respectively) or Hubble's discovery of an expanding Universe (Hubble, 1929), among others. The theory of a non-baryonic, *dark* matter component as part of the total energy content in the Universe extends this list further, owing to the fact that, to this day, no dark matter particle has ever been observed directly. First mentions of dark matter are attributed to Poincaré (1906)[1], Kapteyn (1922) and, most importantly, the famous work by Zwicky (1933), with his redshift studies of extragalactic nebulae such as the Coma, Perseus and Virgo clusters. Since then, physicists endeavoured to decipher the mystery that is dark matter.

Over the years a variety of models have emerged, with particle velocities ranging from the non-relativistic to the fully relativistic limit, and their masses spanning over several magnitudes. Others have tried to modify Newtonian laws of gravity (known as MOND, see Milgrom (1983)) to account for the gravitational effects identified in observations, which we will not discuss further. Dark matter models base their assumptions on the existence of hypothetical particles such as the axion (Peccei and Quinn (1977), Weinberg (1978), Wilczek (1978)), supersymmetric and weakly interacting massive particles (WIMPs, see Goldberg (1983), Ellis et al. (1984) for early work, and Jungman et al. (1996) for a comprehensive review), ultralight bosons and many others. Although dark matter in form of an elementary particle is favoured nowadays, it was further proposed that primordial black holes (PBHs) could contribute to the total amount of dark matter in the Universe (see, e.g., Carr and Kühnel (2020) for a recent review). For an extensive review on the history of dark matter we refer to Bertone and Hooper (2018), a summary of dark matter models from a particle physics' point of view is further given in Bertone et al. (2005).

While experimentalists aim to ultimately detect dark matter particles through construction and usage of detectors with ever-growing precision, it is

[1] In his original work, written in French, he used the term *matière obscure*.

the task of theorists to conceive and to narrow down the possible parameter space for the numerous proposed candidates. This work aims to examine the response of dark matter particles due to baryonic infall in galactic haloes in a theoretical manner, based on early work by Blumenthal et al. (1986) (see also, e.g., Barnes and White (1984), Ryden and Gunn (1987), Gnedin et al. (2004)). However, while this so-called *adiabatic contraction* model has been applied extensively in the context of the ΛCDM paradigm (see Section 1.2), it shall now be extended to scalar field dark matter (SFDM) cosmologies, including a thorough analysis of the underlying Quantum-Hamilton-Jacobi framework appropriate for SFDM, and the notion of orbits, in order to verify the validity of the assumptions usually required for adiabatic contraction.

The remainder of this chapter is dedicated to motivate the study of dark matter, i.e. it covers various independent evidence for its existence, followed by an introduction into today's Standard Model of Cosmology, the aforementioned ΛCDM model, and its ongoing small-scale crisis. The chapter then concludes with a brief introduction to four nowadays popular dark matter models, each in stark contrast to the others, and to structure formation. Chapter 2 covers the analytical calculation of individual important quantities for the SFDM model. The calculation of orbits in this model, expressed in action-angle variables, and their visualization, achieved through numerical calculation, are presented in Chapter 3. Chapter 4 introduces the framework and results for adiabatic contraction in SFDM, and Chapter 5 finally summarises and discusses the findings.

1.1 Evidence for dark matter

While there is much observational evidence for dark matter, discussing all of it would exceed the scope of this thesis. Thus, from the three examples presented here, each represents evidence on a different physical scale. Following Bertone et al. (2005), we shall commence with the galactic scale and then subsequently examine larger cluster and cosmological scales.

Rotation curves of spiral galaxies Rubin and Ford (1970) were among the first publications dedicated to the study of these rotation curves. They analyzed spectra of 67 HII regions from M31's nucleus and found rotation curves that are rapidly rising in the inner parts of the galaxy, but flatten at larger distances from the center. Rogstad and Shostak (1972) further investigated HI surface densities and rotation curves of five Scd galaxies. A comparison of those quantities revealed that, although the bulk of neutral hydrogen gas is located in the inner regions of the galaxies, the rotation curves again rise rapidly and then flatten in the outer regions. A third, concurrent study by Roberts and Rots (1973) observed the same phenomenon, although comparing spiral galaxies of different types (i.e. Sb, Scd and Sab), thus confirming this picture.

Newtonian dynamics teaches us that the (circular) velocity for an object situated in a gravitational field follows

$$v_{\mathrm{circ}}(r) = \sqrt{\frac{GM(r)}{r}}, \tag{1.1}$$

where G is the gravitational constant and $M(r)$ is the enclosed mass at radius r. Applying this equation to baryonic matter, i.e. stars, gas and dust, in spiral galaxies, we were to expect an initial peak followed by a drop-off in velocity for increasing radius - in contradiction to the observations described above. However, if a surrounding dark matter halo is considered, with the galaxy located in its center, equation (1.1) reproduces the characteristic flat rotation curve, as visualized for several NGC galaxies in Begeman et al. (1991).

Gravitational lensing Based on Einstein's theory of general relativity we know that light bends, or more precisely, that photons travel through warped space-time when passing a gravitational well, e.g. that of our Sun, a galaxy or even massive galaxy clusters. His findings were first observed during a total solar eclipse in 1919, which allowed astronomers to observe light from stars near the Sun which were slightly out of position compared to the case without light bending (Dyson et al., 1920). Since then, gravitational lensing has been used extensively to study distant galaxies lying directly or partly behind, for example, clusters. This effect is called *strong lensing*, since it requires massive amounts of matter as lensing object; these high masses can thus result in distortions like arcs, Einstein rings or even multiple images of the lensed galaxy. A review of this phenomenon is given in Treu (2010). However, the extent of these distortions can not be fully accounted for by the amount of luminous matter alone, hinting once more to the existence of dark matter.

Apart from strong lensing, there is an additional, statistical effect, denoted as *weak lensing*. Recently, the Dark Energy Survey (DES)[2] has used this effect to reconstruct a map of all matter for a large portion of the sky. Because it is believed that dark matter outweighs baryonic matter by a factor of 5 (see Section 1.2), this map shows the distribution of dark matter and can be used for comparison to optical galaxy surveys for further studies (DES Collaboration, 2021).

Cosmic Microwave Background (CMB) The last example is one with arguably the most considerable consequences. As a remnant of an early stage of the Universe, originated approximately 380,000 years after the Big Bang in an epoch of recombination, the CMB allows physicists to infer information about content, geometry and evolution of the cosmos. It was first measured by Penzias and Wilson (1965) as an excess temperature of 3.5 ± 1 K; follow-up observations by satellites like COBE, WMAP and Planck narrowed this temperature down to 2.72548 ± 0.00057 K (see, e.g., Fixsen (2009), Planck Collaboration (2020)).

[2] `https://www.darkenergysurvey.org/`

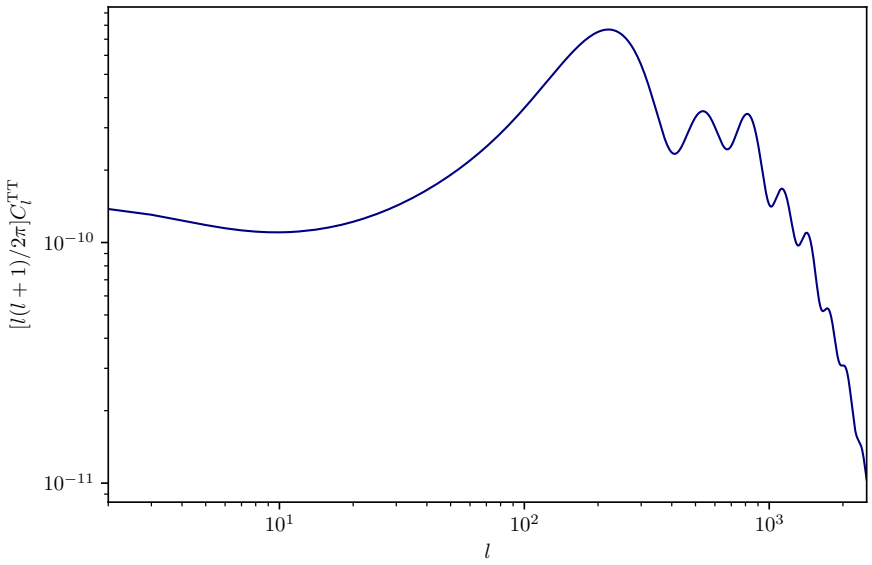

Figure 1.1: CMB temperature power spectrum (TT) as a function of mode number l, reproduced with help of the CLASS code (Lesgourgues (2011), Blas et al. (2011)) and based on Planck Collaboration (2020) data. The positions and heights of the various peaks, absolute and relative to each other, provide remarkably accurate information about history and nature of the Universe.

The mathematical framework behind CMB data is not trivial and beyond the scope of this thesis, the reader is therefore referred to Planck Collaboration (2020), and references therein, for a deeper dive into this topic. However, publicly available codes like CLASS[3] enable researchers to easily examine the Planck data and experiment with other cosmological parameters (see, e.g., Rindler-Daller (2020)). Figure 1.1 shows the CMB TT temperature power spectrum based on parameters from Planck Collaboration (2020) and obtained through

$$C_l = \frac{1}{2l+1} \sum_{m=-l}^{l} \langle |a_{lm}|^2 \rangle,$$

with multipole mode number l and expansion coefficients a_{lm}. From this, one can deduce, for example, the energy content of the Universe as we know it today, with matter densities $\Omega_c h^2 = 0.1200 \pm 0.0012$ for dark matter and $\Omega_b h^2 = 0.02237 \pm 0.00015$ for baryonic matter.

[3] `https://lesgourg.github.io/class_public/class.html`

1.2 The Standard Model and its small-scale problems

As mentioned above, there is a variety of dark matter models available today. The earliest attempts attributed the missing mass to heavy neutrinos with $m \sim 30$ eV (see, e.g., Zel'dovich et al. (1982), Shandarin et al. (1983)), nowadays called *hot dark matter*. Although promising at first, the theory was later more or less discarded due to its inability to correctly describe observations - in hot dark matter cosmologies structure would form slowly and "top down", i.e. large structures form first, followed by smaller structures. In reality, hierarchical structure formation prevails, where small structures like galaxies form earlier than larger ones like galaxy clusters, in a "bottom up" manner. One theory is able to reproduce these observations, among numerous others, exceptionally well - *cold dark matter*[4]. In this theory the dark matter particles are described as a collisionless, non-relativistic and non-baryonic gas. Accompanied with the cosmological constant Λ, the model grants us the best description of the Universe we have today - the Standard Model of Cosmology, or ΛCDM model. Assuming a flat space-time geometry, the model yields the matter components as described in the previous section; furthermore, the power-spectrum of primordial density fluctuations is almost scale-invariant and pressureless cold dark matter collapses under its own gravity, thus creating the gravitational wells into which baryons can fall to form galaxies, clusters and the cosmic web.

Although the ΛCDM model is particularly successful in the description of objects on large scales, the question of which particle dark matter consists of is still an unsolved riddle. The Standard Model of Particle Physics does not provide candidates for dark matter. This ultimately led to the theory of weakly interacting massive particles (WIMPs) with masses in the range of $m \sim 10 - 1000$ GeV, which were tested by Peebles (1982) in the context of large-scale anisotropy of the CMB. Another promising option would be the QCD (quantum chromodynamics) axion with $m \sim 10^{-5} - 10^{-3}$ eV, postulated as a solution to the strong CP problem (Peccei, 2008). While the quest for dark matter particle detection persists, simulations further revealed discrepancies on small scales between observations and predictions. Aptly termed *small-scale crisis of cosmology*, these problems are subject of current research and shall be presented in the following.

Cusp-core problem Observations of gas-rich dwarf galaxies and Low Surface Brightness galaxies (LSBs) suggest dark matter density profiles with approximately constant value in the central parts of the galaxies - so-called cored profiles. However, Navarro et al. (1996) carried out N-body simulations of CDM and identified cuspy density profiles for haloes and their subhaloes, thus resulting in an overprediction of cold dark matter at small radii. Figure

[4]The terms "hot" and "cold" refer here to the velocities of dark matter particles, i.e. hot particles travel with roughly the speed of light c, while cold particles are non-relativistic. Note that intermediate particle velocities are denoted as "warm", which are also studied as potential dark matter theories (Bond et al. (1982), Blumenthal et al. (1982))

2.1 visualizes this universal NFW profile (see also equation (4.5)),

$$\rho(r) = \frac{\rho_s}{\frac{r}{r_s}\left(1+\frac{r}{r_s}\right)^2}, \tag{1.2}$$

with reference density $\rho_s = 1$ and scale radius $r_s = 1$, alongside the cored profile of an $(n = 1)$-polytrope, thus displaying the essence of the problem. A comprehensive overview thereof is given in de Blok (2010).

Missing satellites problem The close to scale-invariant matter power spectrum gives rise to a high amount of substructure in the low-mass regime, the aforementioned subhaloes, which collapse prior to their more massive hosts but still preserve their identities when falling into larger systems (Weinberg et al., 2015). Given the role these subhaloes play in the formation of baryonic structures, one would expect an almost equal amount of satellite galaxies around larger ones, e.g. the Milky Way. According to Klypin et al. (1999), systems with masses comparable to our host galaxy are predicted to be surrounded by roughly 50 satellites, while (at the time the paper was published) only about a dozen have been observed around the Milky Way. They further conclude an even larger discrepancy when considering the observed satellites in the Local Group. However, Weinberg et al. (2015) argue that this problem should be solved comparatively easily by baryonic physics, i.e. suppression of gas accretion onto haloes through the ultraviolet photoionizing background or gas outflow due to supernovae and stellar winds.

Too big to fail problem This issue also concerns satellite galaxies, albeit concentrated on the brightest ones. Boylan-Kolchin et al. (2012) found a disagreement between subhaloes in the Aquarius simulations and the most luminous dwarf spheroidal galaxies around the Milky Way. In order to match the luminosity function of our galaxy, dark matter subhaloes of these dwarf spheroidals with masses ~ 5 times larger than observed are necessary. Moreover, ΛCDM underpredicts infall masses of these galaxies based on their luminosities; this further implies star formation efficiencies that are not compatible with that obtained from more massive galaxies. More recent studies like Kaplinghat et al. (2019) were able to utilize Gaia[5] data of satellite spheroidals to reassess the too big to fail problem. They found an anticorrelation between central dark matter densities of these galaxies and their orbital perimeter distances and were not able to resolve the problem, but instead constrain proposed solutions.

1.3 Alternatives to the ΛCDM paradigm

Extensive research and effort is required in the future in order to unravel the questions raised by dark matter - however, a variety of approaches are available

[5] `https://sci.esa.int/web/gaia`

for astrophysicists to solve this mystery. Many people aim to further develop the ΛCDM model to tackle the small-scale problems via baryonic feedback (Bullock and Boylan-Kolchin, 2017). Others, on the other hand, attempt different approaches to find better descriptions of the Universe - the development of new theories. While some of these provide promising dark matter candidates, or at least could describe a portion of it, these newer theories must withstand exact scrutiny in order to possibly dethrone ΛCDM as the Standard Model. Thus, they must correctly reproduce observations already described by ΛCDM, while simultaneously give accurate predictions where the Standard Model is unable to. We briefly present four alternative, fundamentally different models currently researched.

Primordial Black Holes (PBHs) Earliest work on this topic was done by Zel'dovich and Novikov (1967), who argued that objects with radii shorter than the Schwarzschild radius,

$$r_S = \frac{2GM}{c^2},$$

would lead to strong accretion of radiation if occurring at early stages of expansion. Depending on the time of formation, these black holes could have masses in the range of the Planck mass, $m_P = \sqrt{\hbar c/G} = 2.176434 \cdot 10^{-5}$ g, if formed at the Planck time ($\sim 10^{-43}$ s), or around $10^5\, M_\odot$ if formed just one second after the Big Bang (Carr and Kühnel, 2020). Although these black holes still belong to the family of cold dark matter theories, their lower mass limit of

$$M_{\mathrm{PBH}} > 10^{-18}\, M_\odot > 10^{39}\ \mathrm{GeV}$$

would be substantially heavier than any potential WIMP particle - by a factor of 10^{36} for even the heaviest WIMP (Frampton, 2016). There are numerous ways PBHs could have formed, as summarized in Carr and Kühnel (2020), ranging from the most natural possibility, primordial inhomogeneities, to inflationary fluctuations or cosmic loops (Hawking, 1989). Current research is dedicated to constraints for PBHs; these constraints may come from evaporation, lensing, dynamics and others.

Self-interacting dark matter (SIDM) Another possibility to resolve the cusp-core and missing satellite problems was proposed by Spergel and Steinhardt (2000). In contrast to collisionless cold dark matter, here they assume a substantial scattering cross-section but negligible dissipation and annihilation, thus allowing the dark matter particles to self-interact with each other. With an estimated range for this cross-section of

$$\frac{\sigma}{m} = 0.45 - 450\ \mathrm{cm}^2\ \mathrm{g}^{-1},$$

it was possible to predict promising properties of galaxies, such as cored, spherical halo centers and fewer dwarf galaxies in groups compared to standard CDM.

More recently, Egana-Ugrinovic et al. (2021) studied the evolution of dark matter perturbations in SIDM cosmologies, yielding matter power spectra for a range of possible cross-sections. While bounds on SIDM velocity-dependent cross sections are yet to be explored through strong lensing, stellar streams or counts of Milky Way satellites, they highlight Lyman-α bounds as the most important probe for future research in this field.

Modified Newtonian dynamics (MOND) The basic principle of this theory is the modification of Newton's second law, $\mathbf{F} = m\mathbf{a}$, describing the force, $\mathbf{F}$, as mass times acceleration, $\mathbf{a}$. When introducing the acceleration constant a_0, which describes the transition from Newtonian to MOND regimes, as well as the interpolating function $\mu(x)$, the adapted force equation reads

$$\mathbf{F} = m\mu\left(\frac{a}{a_0}\right)\mathbf{a}.$$

Evidently, $\mu(x) \to 1$ is necessary for $x \gg 1$ in order to restore Newtonian dynamics, while $\mu(x) \to x$ for $x \ll 1$ must hold for observations on astronomical scales. Famaey and Binney (2005) tested different analytical interpolating functions to produce Milky Way's rotation curve, though only numerically specified functions were able to create circular velocities of $v_{\mathrm{circ}}(R_0) = 220$ km s^{-1} at the Sun's galactocentric radius, R_0. Interestingly, Hossenfelder and Mistele (2019) showed that so-called superfluid dark matter is able to create an additional force, resulting in similar effects as MOND.

Scalar field dark matter (SFDM) Here it is assumed that dark matter is comprised of scalar bosons, thus spin-0 particles, which possibly experience self-interaction (Li et al., 2014). A prominent candidate for this kind of dark matter is the QCD axion with weak attractive self-interaction. Current astronomical observational constraints allow an axion mass of around $\sim 10^{-5}$ eV, which would result in structure formation comparable to that of standard CDM, including the small-scale problems as well. However, extensions to the Standard Model of Particle Physics also predict ultra-light axions (also axion-like particles, ALPs), with a lower mass bound of $m > 10^{-33}$ eV (Li et al., 2017). The upper limit is set by the particles' de Broglie wavelength, which determines the scale below which structure formation is restrained. For example, for non-interacting ALPs, a mass of 10^{-18} eV makes them indistinguishable from CDM with regard to the CMB. The bosons of SFDM either form haloes by Bose-Einstein condensation of the scalar field (Magaña and Matos, 2012), or are initially in a Bose-Einstein condensate (Li et al., 2017). For the remainder of this thesis we will focus our attention on this dark matter theory, with Chapter 2 giving a more detailed analysis of the topic.

1.4 Structure formation

As mentioned above, the ΛCDM model suggests that structure forms hierarchically. Starting from the initial perturbations in the early Universe, small density fluctuations create the seeds for subsequent structure formation. This process depends strongly on the amount of dark matter in the Universe, i.e. other distributions of the total energy content would alter the positions, and absolute and relative heights of the peaks in Figure 1.1. In areas with slight overdensities, compared to the mean, more particles accumulate and form gravitational wells. Under the influence of gravity these wells then evolve into the dark matter haloes which can be observed and simulated today. In turn, their gravitational influence also acts on baryons, dragging them to their very centers to create galaxies. While large-scale cosmological simulations use the N-body approach to investigate these interactions, there are also more simple (in regard to baryon physics), approximate models like adiabatic contraction. Based on the conservation of angular momentum, this model calculates the response of dissipationless dark matter particles inside a halo to the presence of baryonic matter situated in the center of the halo. In the light of Milky Way data, Cautun et al. (2020) discuss that most studies ignore this effect despite a change in density in the inner 10 kpc, essentially leading to flawed mass estimates of our Galaxy. However, as this thesis is focused on SFDM and especially on the small-scale problems, we shall investigate in Chapter 4 the effects of adiabatic contraction on SFDM dark matter halo densities and rotational velocities on the scale of dwarf galaxies.

Chapter 2

Scalar field dark matter

Alongside the above discussed alternatives to the ΛCDM paradigm stands another theory, namely scalar field dark matter. As it forms the core of this thesis, it deserves a whole chapter, which will be dedicated to its underlying framework and its resulting consequences. Early work on this topic was done by Baldeschi et al. (1983), who considered galactic haloes consisting of massive fermions and bosons, the latter having a mass in the range of $10^{-24} - 10$ eV. Further studies, for example by Hu et al. (2000), have investigated the wave properties of this dark matter candidate composed of *ultra-light scalar particles*. More precisely, these bosons with masses of $m \sim 10^{-22}$ eV behave in a comparable way to standard CDM on large scales, while suppressing structure formation on small, subgalactic scales. This is due to their small mass and their non-relativistic velocity v, resulting in the particles' de Broglie wavelength,

$$\lambda_{\mathrm{deB}} = \frac{h}{mv},$$

becoming relevant on astronomical scales,

$$\lambda_{\mathrm{deB}} = 12.06 \left(\frac{10^{-22}\ \mathrm{eV}}{m}\right) \left(\frac{10\ \mathrm{km\ s^{-1}}}{v}\right)\ \mathrm{kpc}.$$

Ultra-light bosons are able to undergo a phase transition in the early Universe to a Bose-Einstein condensate (BEC), thus occupying a single macroscopic quantum state, the ground state, and ultimately leading to self-gravitating Bose-Einstein condensed haloes (see, e.g., Rindler-Daller and Shapiro (2012) and references therein)[1].

Since its proposal as potential dark matter candidate, great effort has been made in order to narrow down the range of the boson mass, e.g. through Lyman-α forest constraints (Amendola and Barbieri, 2006), or from reionization and UV-luminosity function comparisons at high redshift (Schive et al., 2016). Others inferred the mass from dwarf galaxy rotation curves inside the Local

[1] Because of its wave-like nature and description as a Bose-Einstein condensate, scalar field dark matter is also called wave dark matter or BEC dark matter in the literature.

Group (Robles and Matos, 2013) and performed cosmological simulations to study turbulence and relaxation of BEC haloes as well as cosmic filaments (Mocz et al. (2017), Mocz et al. (2020)). While many of these works neglected self-interaction between particles, recent studies shed more light on the regime with strong repulsive self-interaction, specifically in the context of the small-scale problems (Dawoodbhoy et al., 2021). In order to obtain a better understanding of SFDM, the subsequent sections will provide step-by-step calculations based upon a few key assumptions.

2.1 Fundamental equations

In this theory the behaviour of self-gravitating BEC haloes can be formulated through a non-linear Schrödinger equation,

$$i\hbar\frac{\partial\psi(\mathbf{r},t)}{\partial t} = -\frac{\hbar^2}{2m}\Delta\psi(\mathbf{r},t) + \left(m\Phi(\mathbf{r},t) + g|\psi(\mathbf{r},t)|^2\right)\psi(\mathbf{r},t), \tag{2.1}$$

where m is the boson mass. This equation describes the evolution of the scalar field $\psi(\mathbf{r},t)$ in an external potential, in this case a time-dependent gravitational potential $\Phi(\mathbf{r},t)$, while simultaneously experiencing two-body interactions between the particles. The strength of this self-interaction is characterized by the coupling constant g, which can be either repulsive or attractive. Since attractive self-interaction does not suppress small-scale structure it will not be considered in this thesis. In order to be repulsive, the coupling constant must satisfy

$$g = \frac{4\pi\hbar^2 a_s}{m} > 0, \tag{2.2}$$

where a_s represents the s-wave scattering wave length (Rindler-Daller and Shapiro, 2012). The original form of equation (2.1) was developed independently by Gross (1961) and Pitaevskii (1961) and is thus suitably called Gross-Pitaevskii equation (see, e.g., also Pitaevskii and Stringari (2003) for a thorough and more general overview of Bose-Einstein condensation). The repulsive interaction gives rise to a "self-interaction pressure"

$$P_{\mathrm{si}} = K_\rho\rho^{1+1/n} = \frac{g\rho^2}{2m^2}, \tag{2.3}$$

which takes the form of a polytropic equation of state with $n = 1$ and where $K_\rho = g/2m^2$ is the polytropic constant. Furthermore, the Newtonian gravitational potential obeys the Poisson equation,

$$\Delta\Phi(\mathbf{r},t) = 4\pi G\rho(\mathbf{r},t), \tag{2.4}$$

with $\rho(\mathbf{r},t) = m|\psi|^2$ being the dark matter halo mass density; together with equation (2.1) this set is sometimes referred to as the Gross-Pitaevskii-Poisson

(GPP) equations. In order to obtain a closed system of bosons that form a Bose-Einstein condensate, the wave function requires a normalization such that

$$\int_V |\psi|^2 = N$$

is true for the total number of particles N inside the halo volume V.

It is possible to rewrite the GP equation (2.1) as hydrodynamic equations similar to the classical case, i.e. a continuity equation and an (Euler) momentum equation. Though, due to the bosons' quantum-mechanical nature, they are also more aptly called equations of "quantum hydrodynamics" (QHD). This can be accomplished through decomposition of the wave function into its phase function and its amplitude, yielding the so-called Madelung representation (Madelung, 1927) in polar form,

$$\psi(\mathbf{r},t) = |\psi(\mathbf{r},t)|e^{iS(\mathbf{r},t)/\hbar} = \sqrt{\frac{\rho(\mathbf{r},t)}{m}}e^{iS(\mathbf{r},t)/\hbar}, \tag{2.5}$$

in which $S(\mathbf{r},t)$ represents the action function. Inserting this expression into the GP equation leads to

$$i\hbar\frac{\partial}{\partial t}|\psi|e^{iS/\hbar} = -\frac{\hbar^2}{2m}\Delta|\psi|e^{iS/\hbar} + \left(m\Phi + g|\psi|^2\right)|\psi|e^{iS/\hbar}.$$

While the left-hand side of this equation can be rewritten as

$$i\hbar\frac{\partial}{\partial t}|\psi|e^{iS/\hbar} = i\hbar\left(e^{iS/\hbar}\frac{\partial}{\partial t}|\psi| + |\psi|\frac{\partial}{\partial t}e^{iS/\hbar}\right) = i\hbar e^{iS/\hbar}\left(\frac{\partial|\psi|}{\partial t} + \frac{i|\psi|}{\hbar}\frac{\partial S}{\partial t}\right),$$

rearrangement of the first term on the right-hand side results in

$$\begin{aligned}-\frac{\hbar^2}{2m}\Delta|\psi|e^{iS/\hbar} &= -\frac{\hbar^2}{2m}\left(|\psi|\Delta e^{iS/\hbar} + 2\nabla|\psi|\nabla e^{iS/\hbar} + e^{iS/\hbar}\Delta|\psi|\right)\\ &= -\frac{\hbar^2}{2m}e^{iS/\hbar}\left(|\psi|\left[\frac{i}{\hbar}\Delta S - \frac{1}{\hbar^2}\left(\nabla S\right)^2\right] + \frac{2i}{\hbar}\nabla|\psi|\nabla S + \Delta|\psi|\right).\end{aligned}$$

Evidently, the exponentials on both sides cancel out, effectively leading to

$$\begin{aligned}i\hbar\frac{\partial|\psi|}{\partial t} - |\psi|\frac{\partial S}{\partial t} = -\frac{\hbar^2}{2m}|\psi|\left(\frac{i}{\hbar}\Delta S - \frac{1}{\hbar^2}(\nabla S)^2\right) - \frac{i\hbar}{m}\nabla|\psi|\nabla S - \frac{\hbar^2}{2m}\Delta|\psi|\\ + |\psi|\left(m\Phi + g|\psi|^2\right).\end{aligned} \tag{2.6}$$

This equation can be further decoupled into real and imaginary part; both must equal zero in order to satisfy the equation globally. The imaginary part multiplied by $2|\psi|/i\hbar$ then reads

$$2|\psi|\frac{\partial|\psi|}{\partial t} + \frac{1}{m}|\psi|^2\Delta S + \frac{2}{m}|\psi|\nabla|\psi|\nabla S = 0,$$

which, by making use of product and chain rules, finally yields

$$\frac{\partial|\psi|^2}{\partial t} + \nabla\left(\frac{1}{m}|\psi|^2\nabla S\right) = 0. \tag{2.7}$$

It is useful here to define the bulk velocity (i.e. the average flow velocity) of the halo as

$$\mathbf{v} = \frac{1}{m}\nabla S, \tag{2.8}$$

with which expression (2.7) can be brought into the form of the desired continuity equation,

$$\frac{\partial\rho}{\partial t} + \nabla\cdot(\rho\mathbf{v}) = 0. \tag{2.9}$$

Furthermore, the real part of equation (2.6) can be multiplied by $|\psi|$, resulting in

$$-|\psi|^2\frac{\partial S}{\partial t} + \frac{\hbar^2}{2m}|\psi|\Delta|\psi| - \frac{1}{2m}|\psi|^2(\nabla S)^2 - m\Phi|\psi|^2 - g|\psi|^4 = 0,$$

or, in terms of the dark matter halo density,

$$-\frac{\rho}{m}\frac{\partial S}{\partial t} + \frac{\hbar^2}{2m}\sqrt{\frac{\rho}{m}}\Delta\sqrt{\frac{\rho}{m}} - \frac{\rho}{2m^2}(\nabla S)^2 - \rho\Phi - \frac{g\rho^2}{2m^2} = 0.$$

The second term in this expression can be identified as the so-called quantum potential (Bohm, 1952), causing a "quantum pressure" that emerges from the quantum-mechanical uncertainty principle; it is defined as

$$Q = -\frac{\hbar^2}{2m^2}\frac{\Delta\sqrt{\rho}}{\sqrt{\rho}}. \tag{2.10}$$

Applying ∇, dividing by ρ and making use of bulk velocity, eq. (2.8), and self-interaction pressure, eq. (2.3), the final result yields the Euler-like equation of motion

$$\frac{\partial\mathbf{v}}{\partial t} + (\mathbf{v}\cdot\nabla)\mathbf{v} = -\nabla Q - \nabla\Phi - \frac{1}{\rho}\nabla P_{\mathrm{si}}. \tag{2.11}$$

Equations (2.9) and (2.11) represent a system of quantum-mechanical hydrodynamic equations and are helpful to compare SFDM to other candidates for dark matter, notably standard CDM, which is based upon the collisionless Boltzmann equation (also Vlasov equation) that leads to the Jeans equations. Unlike CDM without self-interactions, the set of QHD equations reveals fluid-like properties for haloes consisting of Bose-Einstein condensate (Rindler-Daller and Shapiro, 2012). The remainder of this chapter is dedicated to the study of

static systems, thus $\partial/\partial t = 0$ and $\mathbf{v} = \mathbf{0}$, in spherical symmetry. Hence, the left-hand side of the Euler equation vanishes and therefore reduces to

$$\nabla Q + \frac{1}{\rho}\nabla P_{\mathrm{si}} = -\nabla\Phi, \tag{2.12}$$

showing that the combination of quantum potential and self-interaction pressure act against the gravitational potential. SFDM allows two regimes serving as limiting cases, one being the so-called *Thomas-Fermi regime*, in which self-interaction pressure exceeds the pressure of the quantum potential ($P_{\mathrm{si}} \gg Q$), the other one denoted as *fuzzy dark matter* (FDM) in the literature, where self-interactions are negligible and Q is the dominant factor against gravity ($P_{\mathrm{si}} \ll Q$). Both have been researched extensively in recent years and shall thus be presented hereafter, with a thorough calculation of key quantities.

2.2 Thomas-Fermi regime

Let us start with the Thomas-Fermi (TF) approximation, where repulsion of the bosons balances gravitational attraction, since this is the regime of interest in this thesis.

Setting $Q = 0$ further reduces equation (2.12) to

$$\frac{1}{\rho}\nabla P_{\mathrm{si}} = -\nabla\Phi, \tag{2.13}$$

an equivalent to the Lane-Emden equation, as will be shown in the forthcoming.

Density profile Multiplying by r^2 and taking the derivative with respect to r yields

$$\frac{\mathrm{d}}{\mathrm{d}r}\left(\frac{r^2}{\rho}\frac{\mathrm{d}}{\mathrm{d}r}P_{\mathrm{si}}\right) = \frac{\mathrm{d}}{\mathrm{d}r}\left(\frac{r^2}{\rho}\frac{\mathrm{d}}{\mathrm{d}r}\frac{g}{2m^2}\rho^2\right) = -r^2\Delta\Phi,$$

which enables the use of Poisson's equation (2.4), leading to

$$\frac{1}{r^2}\frac{\mathrm{d}}{\mathrm{d}r}\left(r^2\frac{g}{m^2}\frac{\mathrm{d}\rho}{\mathrm{d}r}\right) = -4\pi G\rho. \tag{2.14}$$

This can be solved using the substitutions

$$r = \alpha z, \quad \mathrm{d}r = \alpha \mathrm{d}z, \qquad \text{where} \qquad \alpha = \left(\frac{n+1}{4\pi G}K_\rho \rho_0^{\frac{1}{n}-1}\right)^{1/2} = \left(\frac{K_\rho}{2\pi G}\right)^{1/2}$$

for the radius, and

$$\rho(r) = \rho_0\theta^n(z) = \rho_0\theta(z)$$

for the density. As mentioned earlier the self-interaction pressure takes the form of an $(n = 1)$-polytropic equation of state, hence the simplifications in

both substitutions. Furthermore, the central density of the halo is denoted by $\rho(0) = \rho_0$. Inserting these expressions above then returns

$$\frac{2K_\rho\rho_0}{\alpha^2 z^2}\frac{\mathrm{d}}{\mathrm{d}z}\left(z^2\frac{\mathrm{d}\theta}{\mathrm{d}z}\right) = -4\pi G\rho_0\theta \quad \Longleftrightarrow \quad \frac{1}{z^2}\frac{\mathrm{d}}{\mathrm{d}z}\left(z^2\frac{\mathrm{d}\theta}{\mathrm{d}z}\right) + \theta = 0,$$

taking the form of the aforementioned Lane-Emden equation. The associated boundary conditions assure a finite central density and read $\theta(0) = 1$ and $\theta'(0) = 0$. Another substitution,

$$\xi(z) = z\theta, \quad \frac{\mathrm{d}\theta}{\mathrm{d}z} = \frac{\xi' z - \xi}{z^2},$$

leads to

$$\frac{\mathrm{d}}{\mathrm{d}z}\left(z^2\frac{\xi' z - \xi}{z^2}\right) = -z\xi \qquad \Longleftrightarrow \qquad \xi'' + \xi = 0,$$

which can now be solved easily. The general solution to this differential equation is given by

$$\theta(z) = a\frac{\sin(z)}{z} + b\frac{\cos(z)}{z},$$

with the constants a and b still to be determined. To satisfy the boundary conditions, the constants need to be chosen accordingly,

$$\lim_{z\to 0}\theta(z) \stackrel{!}{=} 1 = \lim_{z\to 0}\left[a\frac{\sin(z)}{z} + b\frac{\cos(z)}{z}\right],$$

which can be solved by making use of the rule of L'Hôspital. This results in

$$\lim_{z\to 0}\frac{\sin(z)}{z} = \lim_{z\to 0}\frac{\cos(z)}{1} = 1 \qquad \Rightarrow \qquad a = 1$$

and

$$\lim_{z\to 0}\frac{\cos(z)}{z} = \infty \qquad \Rightarrow \qquad b = 0.$$

The second condition is then automatically fulfilled,

$$\theta'(0) = \lim_{z\to 0}\frac{z\cos(z) - \sin(z)}{z} = \lim_{z\to 0}\frac{-z\sin(z)}{2z} = -\lim_{z\to 0}\frac{\sin(z)}{2} = 0,$$

which is again solved through the usage of L'Hôspital's rule. The solution is therefore of the form $\theta(z) = \sin(z)/z$, or, after backward substitution,

$$\rho(r) = \rho_0\frac{\sin\left(\pi r/R_{\mathrm{TF}}\right)}{\pi r/R_{\mathrm{TF}}}, \tag{2.15}$$

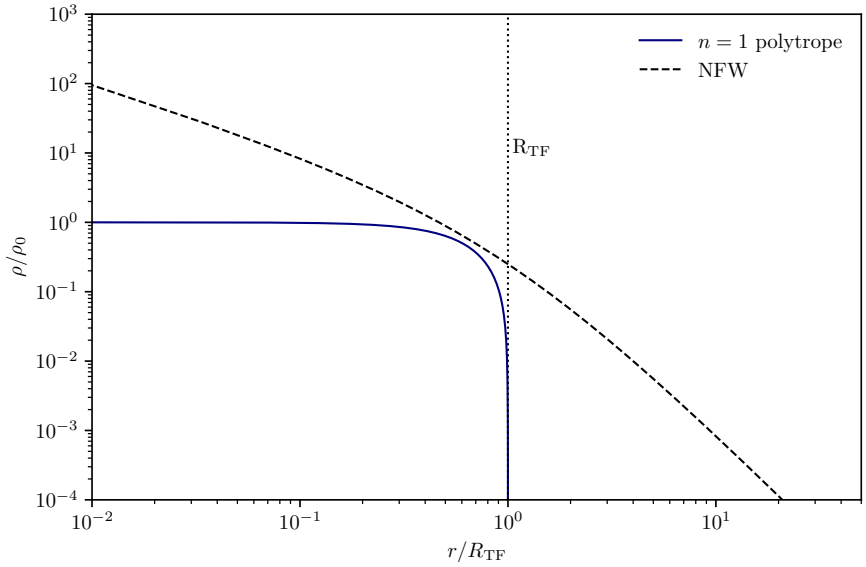

Figure 2.1: The density profile for an $(n = 1)$-polytrope is a typical *cored* profile, i.e. it becomes flat at small radii. In contrast, the NFW profile represents the class of *cuspy* dark matter profiles with increasing density in the inner regions. Note the steep decline of the polytrope density once it approaches the Thomas-Fermi radius.

where the radius of the Thomas-Fermi polytrope, at which the density first vanishes (i.e. at the first zero), is defined as

$$R_{\mathrm{TF}} = \pi\sqrt{\frac{K_\rho}{2\pi G}} = \pi\sqrt{\frac{g}{4\pi G m^2}}. \tag{2.16}$$

It is remarkable that this radius does not depend on the polytrope's total mass, but only on the fundamental dark matter particle parameters of this theory. Figure 2.1 shows the density profile corresponding to equation (2.15) in comparison to a NFW profile, see equation (1.2), with R_{TF} as its scale radius, visualizing the sharp density drop-off at this radius. While these sharp drop-offs are not observed in the Universe, they give a good description for the core regions of dark matter haloes. In fact, as will be shown in Section 2.3, observed and simulated density profiles can be reproduced exceptionally well when embedding these cores in a surrounding envelope.

Gravitational potential Given the density profile, it is now possible to again make use of the Poisson equation to derive the gravitational potential of BEC halo cores in the Thomas-Fermi regime. Thus, inserting equation (2.15) into equation (2.4) gives

$$\Delta\Phi(r) = 4\pi G\rho(r) = 4\pi G\rho_0 \frac{\sin(\pi r/R_{\mathrm{TF}})}{\pi r/R_{\mathrm{TF}}},$$

or, with the Laplacian in spherical symmetry,

$$\frac{\mathrm{d}}{\mathrm{d}r}\left(r^2\frac{\mathrm{d}}{\mathrm{d}r}\right)\Phi = \frac{4\pi G\rho_0 r\sin(\pi r/R_{\mathrm{TF}})}{\pi/R_{\mathrm{TF}}}.$$

Performing simple partial integration leads to

$$\frac{\mathrm{d}\Phi}{\mathrm{d}r} = \frac{4G\rho_0 R_{\mathrm{TF}}}{r^2}\left(\frac{\sin(\pi r/R_{\mathrm{TF}}) - \pi r/R_{\mathrm{TF}}\cos(\pi r/R_{\mathrm{TF}})}{\pi^2/R_{\mathrm{TF}}^2} + c_1\right), \tag{2.17}$$

which needs to be integrated further, though by substitution, to result in

$$\Phi(r) = \frac{4G\rho_0 R_{\mathrm{TF}}^3}{\pi^2}\left(-\frac{\sin(\pi r/R_{\mathrm{TF}})}{r} - \frac{c_1\pi^2/R_{\mathrm{TF}}^2}{r} + c_2\right). \tag{2.18}$$

In order to specify the two integration constants c_1 and c_2 it is necessary to accompany the equation with two boundary conditions. The first condition usually is chosen so that no forces act in the center, thus $\nabla\Phi(r=0)=0$. From expression (2.17) it is evident to use L'Hospital's rule again on the first two terms in the brackets; since both equal zero for $r\to 0$, the necessary condition for the first constant is $c_1 = 0$. The second boundary condition is chosen as $\Phi(r) = -1/r$ for $r\to\infty$, i.e. it should resemble a Kepler potential for large radii. Equation (2.18) then reads

$$-\frac{1}{r} = -\frac{4G\rho_0 R_{\mathrm{TF}}^3}{\pi^2}\left(\frac{\sin(\pi r/R_{\mathrm{TF}})}{r} - c_2\right),$$

where

$$-\frac{4G\rho_0 R_{\mathrm{TF}}^3}{\pi^2}\frac{\sin(\pi r/R_{\mathrm{TF}})}{r} \approx -\frac{\text{const.}}{r} \qquad \text{for} \qquad r\to\infty.$$

For the second condition to be satisfied $c_2 = 0$ is thus required, and the gravitational potential of an $(n=1)$-polytrope in the Thomas-Fermi regime reads

$$\Phi(r) = -\frac{4G\rho_0 R_{\mathrm{TF}}^3}{\pi^2}\frac{\sin(\pi r/R_{\mathrm{TF}})}{r}. \tag{2.19}$$

Enclosed mass & circular velocity For the purpose of this thesis it is also useful to derive the analytic solutions of enclosed mass and rotational velocity of such haloes. Given the already known density profile from equation (2.15), the derivation of these quantities is straightforward. For the enclosed mass an integration suffices to obtain

$$\begin{aligned} M(r) &= \int_0^r 4\pi r'^2\rho(r')\mathrm{d}r' = 4R_{\mathrm{TF}}\rho_0\int_0^r r'\sin(\pi r'/R_{\mathrm{TF}})\mathrm{d}r' \\ &= 4R_{\mathrm{TF}}\rho_0\left[\frac{R_{\mathrm{TF}}^2\sin(\pi r'/R_{\mathrm{TF}}) - \pi R_{\mathrm{TF}} r'\cos(\pi r'/R_{\mathrm{TF}})}{\pi^2}\right]_0^r \\ &= \frac{4R_{\mathrm{TF}}^3\rho_0}{\pi^2}\left(\sin(\pi r/R_{\mathrm{TF}}) - \frac{\pi r}{R_{\mathrm{TF}}}\cos(\pi r/R_{\mathrm{TF}})\right), \end{aligned} \tag{2.20}$$

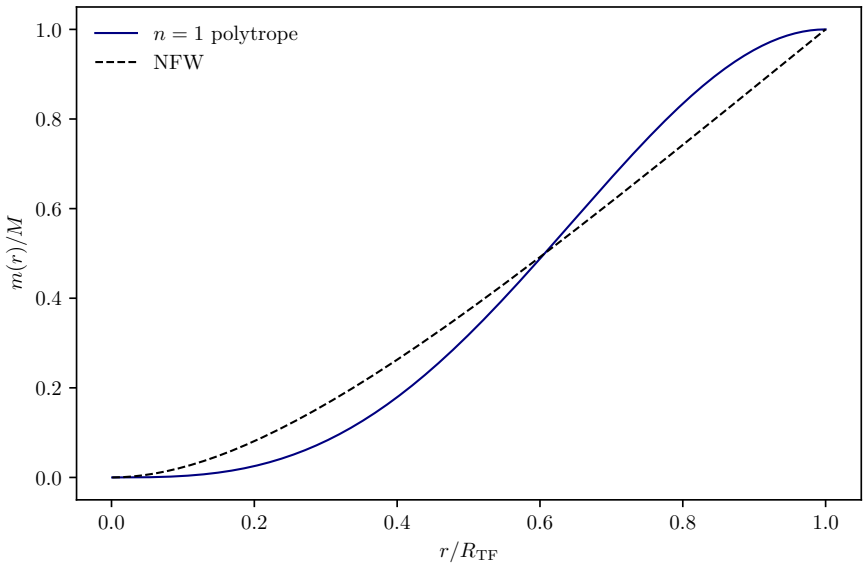

Figure 2.2: Normalized enclosed mass profile of the $(n = 1)$-polytrope, compared to the NFW profile.

which can be seen in Figure 2.2. From this expression the circular velocity can be calculated, resulting in

$$v(r) = \sqrt{\frac{GM(r)}{r}} = \sqrt{\frac{4GR_{\mathrm{TF}}^2\rho_0}{\pi}\left(\frac{R_{\mathrm{TF}}}{\pi r}\sin(\pi r/R_{\mathrm{TF}}) - \cos(\pi r/R_{\mathrm{TF}})\right)} \tag{2.21}$$

and shown in Figure 2.3.

2.3 Double-polytropes: Thomas-Fermi core plus envelope

After deriving quantities concerning the cores of gravitationally bound BEC haloes it is now time to complete the physical picture by embedding them into envelopes modeled by isothermal spheres; this effectively leads to a double-polytrope for the pressure (Dawoodbhoy et al., 2021). The assumption made here is an additional velocity dispersion,

$$\sigma^2 = \frac{P_\sigma}{\rho} = \text{const.}, \tag{2.22}$$

resulting in another polytropic pressure with $n = \infty$ and $K_\rho = \sigma^2$. This assumption is consistent with observations of rotation curves of galaxies within virialized CDM haloes which are close to isothermal. Equation (2.13) is then

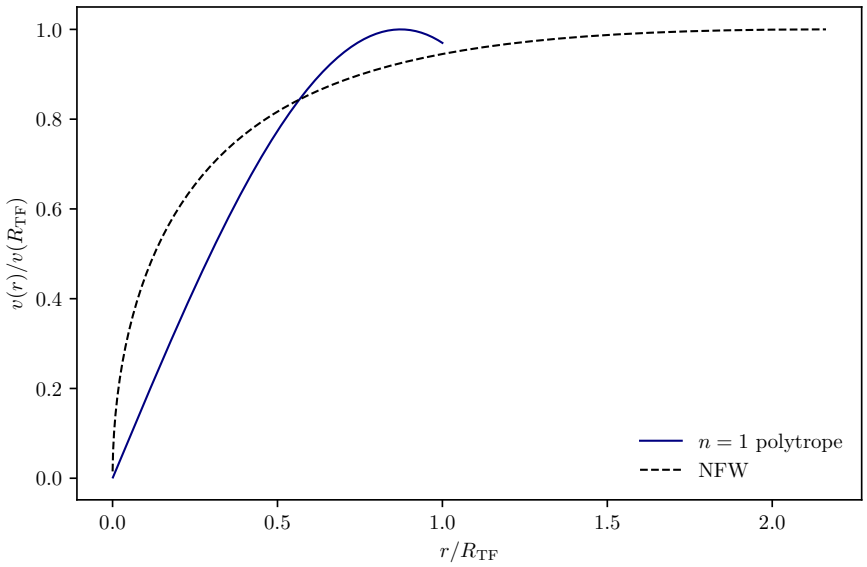

Figure 2.3: Circular velocity curve of the polytrope, obtained by equation (2.21), compared to the NFW profile. Note that for the polytrope, the maximum $v_{\rm max}$ is reached at $\sim 0.85 R_{\rm TF}$, while the NFW profile has its maximum value at $r_{\rm max} \simeq 2.163 R_{\rm TF}$ (which depends on the profile's concentration parameter c; here $c = 1$ is considered).

extended by this pressure and reads

$$\frac{1}{\rho}\nabla\left(P_\sigma + P_{\rm si}\right) = \frac{1}{\rho}\frac{\mathrm{d}}{\mathrm{d}r}\left(\sigma^2\rho + \frac{g}{2m^2}\rho^2\right) = \sigma^2\frac{\mathrm{d}\ln\rho}{\mathrm{d}r} + \frac{g}{m^2}\frac{\mathrm{d}\rho}{\mathrm{d}r} = -\nabla\Phi.$$

As above for the core only, multiplication by r^2 is required, followed by taking the derivative in order to use Poisson's equation for the gravitational potential,

$$\frac{\mathrm{d}}{\mathrm{d}r}\left(\sigma^2 r^2\frac{\mathrm{d}\ln\rho}{\mathrm{d}r} + \frac{g}{m^2}r^2\frac{\mathrm{d}\rho}{\mathrm{d}r}\right) = -4\pi G r^2\rho. \tag{2.23}$$

Evidently, here one can again identify two limiting cases: In the core regions the pressure from particle self-interactions is predominant, the velocity dispersion can therefore be assumed to vanish, $\sigma^2 = 0$, and the remaining equation is consistent with eq. (2.14) and thus corresponds to the Thomas-Fermi regime, appropriate for the central regions of the halo. In contrast, in the surrounding envelope the velocity dispersion prevails and $g = 0$ can be adopted. This solution corresponds to an isothermal sphere, hence eq. (2.23) reads as

$$\frac{\mathrm{d}}{\mathrm{d}r}\left(r^2\frac{\mathrm{d}\ln\rho}{\mathrm{d}r}\right) = -\frac{4\pi G r^2\rho}{\sigma^2}.$$

The density profile obtained by solving this equation yields

$$\rho(r) = \frac{\sigma^2}{2\pi G r^2}, \tag{2.24}$$

while its characteristic radius is given by

$$r_0 = \left(\frac{\sigma^2}{4\pi G\rho_0}\right)^{1/2}.$$

The profile in equation (2.24) describes the halo envelope around the core and corresponds to a flat rotation curve, thus being in agreement with observations. Although there exist analytic solutions for each of the limiting cases of the differential equation (2.23), in general, it can be only solved numerically. This will be done with two different methods, as discussed below, which differ in the way the equation gets non-dimensionalized.

Method 1 To proceed with the calculations it is necessary to introduce two substitutions,

$$\tilde{\rho} = \frac{\rho}{\rho_0}, \qquad \text{and} \qquad \zeta = \frac{r}{R_{\mathrm{TF}}}, \quad \mathrm{d}r = R_{\mathrm{TF}}\mathrm{d}\zeta,$$

with the definition of the Thomas-Fermi radius from equation (2.16). Again, the density in the center of the core is given by $\rho(0) = \rho_0$. Furthermore, the particles' circular velocity at R_{TF},

$$v^2(R_{\mathrm{TF}}) = v_c^2 = \frac{GM_c}{R_{\mathrm{TF}}},$$

will be used, where the enclosed mass M_c at this radius reads

$$M(R_{\mathrm{TF}}) = M_c = \frac{4\rho_0 R_{\mathrm{TF}}^3}{\pi}.$$

The validity of these two expressions can be checked by setting $r = R_{\mathrm{TF}}$ in equations (2.20) and (2.21). At last, a variable which determines the relative strength of the two polytropic regimes can be defined,

$$\kappa = \frac{\sigma^2}{v_c^2}.$$

Inserting these terms into eq. (2.23) leads to

$$\begin{aligned}
\frac{\mathrm{d}}{\mathrm{d}\zeta}\left(\frac{\sigma^2\zeta^2 R_{\mathrm{TF}}^2}{R_{\mathrm{TF}}^2}\frac{\mathrm{d}\ln\tilde{\rho}\rho_0}{\mathrm{d}\zeta} + \frac{g}{m^2}\frac{\rho_0\zeta^2 R_{\mathrm{TF}}^2}{R_{\mathrm{TF}}^2}\frac{\mathrm{d}\tilde{\rho}}{\mathrm{d}\zeta}\right) &= -4\pi G\zeta^2 R_{\mathrm{TF}}^2\tilde{\rho}\rho_0 \\
\frac{\mathrm{d}}{\mathrm{d}\zeta}\left(\sigma^2\zeta^2\frac{\mathrm{d}\ln\tilde{\rho}}{\mathrm{d}\zeta} + \frac{g}{m^2}\zeta^2\rho_0\frac{\mathrm{d}\tilde{\rho}}{\mathrm{d}\zeta}\right) &= -4\pi G\zeta^2 R_{\mathrm{TF}}^2\tilde{\rho}\rho_0 \\
\frac{\mathrm{d}}{\mathrm{d}\zeta}\left(\kappa\zeta^2\frac{\mathrm{d}\ln\tilde{\rho}}{\mathrm{d}\zeta} + \zeta^2\frac{\mathrm{d}\tilde{\rho}}{\mathrm{d}\zeta}\right) &= -\pi^2\zeta^2\tilde{\rho}. \qquad (2.25)
\end{aligned}$$

Together with the boundary conditions $\tilde{\rho}(0) = 1$ and $\tilde{\rho}'(0) = 0$ this second order differential equation can be solved numerically upon rewriting it in terms

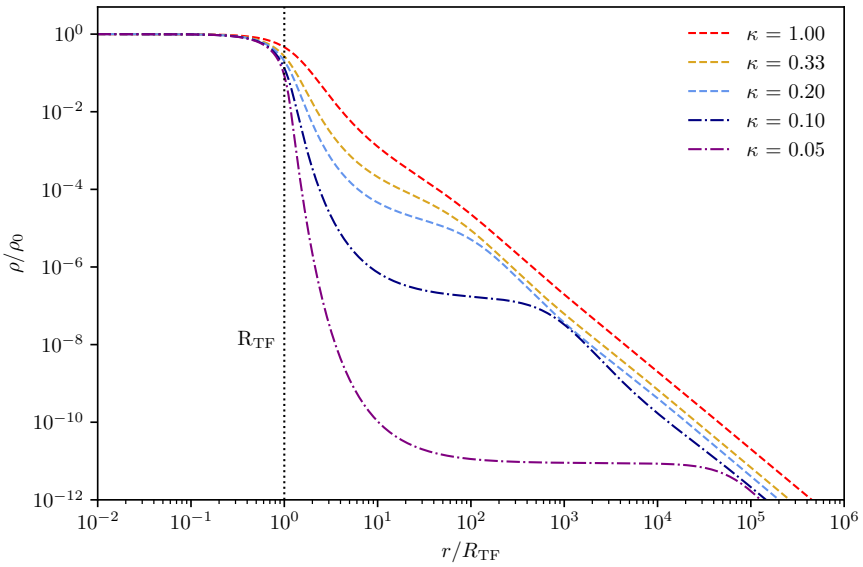

Figure 2.4: Numerical solutions to equation (2.25) with different values for κ. A vertical line at R_{TF} was added for reference. For $\kappa \to 0$, the density profile approaches the solution of the $(n = 1)$-polytrope, equation (2.15).

of a system of first order differential equations. Figure 2.4 shows solutions for five different values of κ.

Method 2 The second method is based upon the substitutions

$$\rho = \rho_0 e^{-\psi} \qquad \text{and} \qquad \xi = \frac{r}{r_0}, \quad \mathrm{d}r = r_0 \mathrm{d}\xi,$$

as was done in Chavanis (2019)[2]. Moreover, using the characteristic radius of the isothermal sphere and the Thomas-Fermi radius, one can define

$$\chi = \left(\frac{R_{\mathrm{TF}}}{\pi r_0}\right)^2 = \frac{\pi^2 g \rho_0}{m k_B T} = \frac{1}{\kappa}.$$

With these definitions equation (2.23) can be written as

$$\begin{aligned}
\frac{\mathrm{d}}{\mathrm{d}\xi}\left(\frac{\sigma^2 r_0^2 \xi^2}{r_0^2}\frac{\mathrm{d}\ln \rho_0 e^{-\psi}}{\mathrm{d}\xi} + \frac{g}{m^2}\frac{r_0^2\xi^2\rho_0}{r_0^2}\frac{\mathrm{d}e^{-\psi}}{\mathrm{d}\xi}\right) &= -4\pi G r_0^2 \xi^2 \rho_0 e^{-\psi} \\
-\frac{\mathrm{d}}{\mathrm{d}\xi}\left(\sigma^2\xi^2\frac{\mathrm{d}\psi}{\mathrm{d}\xi} + \frac{g}{m^2}\xi^2\rho_0 e^{-\psi}\frac{\mathrm{d}\psi}{\mathrm{d}\xi}\right) &= -4\pi G r_0^2 \xi^2 \rho_0 e^{-\psi} \\
\frac{1}{\xi^2}\frac{\mathrm{d}}{\mathrm{d}\xi}\left(\xi^2\frac{\mathrm{d}\psi}{\mathrm{d}\xi} + \chi\xi^2 e^{-\psi}\frac{\mathrm{d}\psi}{\mathrm{d}\xi}\right) &= e^{-\psi}, \qquad (2.26)
\end{aligned}$$

[2]Note that ψ describes only an auxiliary variable here and should not be confused with the bosonic wave function from Section 2.1.

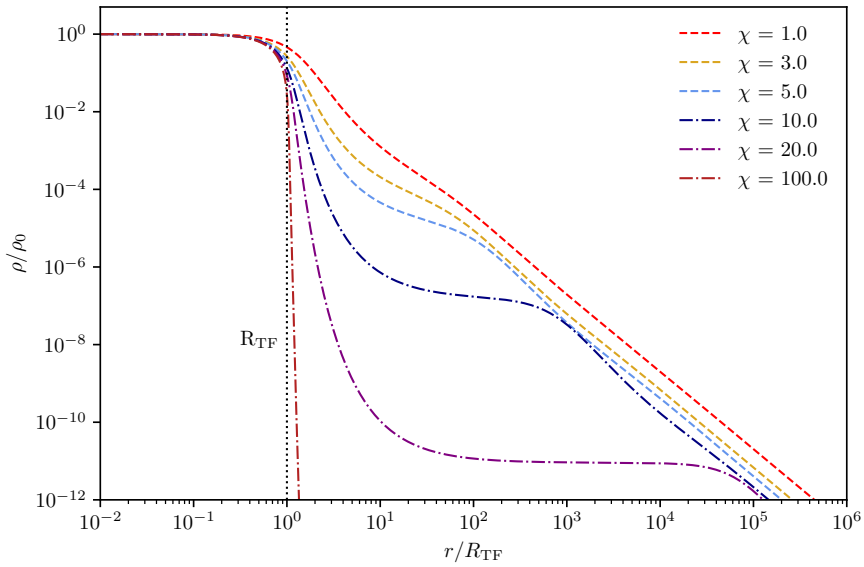

Figure 2.5: Numerical solutions to equation (2.26) with different values for χ. A vertical line at R_{TF} was added for reference. For $\chi \to \infty$, the density profile approaches the solution of the $(n = 1)$-polytrope, equation (2.15). For $\chi \to 0$, the solution becomes that of an isothermal sphere.

complemented with the boundary conditions $\psi(0) = \psi'(0) = 0$. The solution is obtained in the same way as for Method 1, using a numerical solver, and visualized for different χ in Figure 2.5.

A comparison of both methods reveals identical results. However, for very small κ (and thus large χ), Method 1 diverges from the true solution due to numerical instabilities. Although these small values for κ do not represent realistic halo structures due to their sharp density drop-off, this is something to keep in mind with respect to the implementation in further numerical routines (see Chapter 4 and Appendix B).

2.4 Fuzzy dark matter

In the second regime, called fuzzy dark matter (FDM), self-interactions are neglected and only the quantum potential counteracts gravity. This non-interacting limit has been studied extensively in the context of halo formation through collisions of individual, so-called solitonic cores (see, e.g., Schive et al. (2014), Schwabe et al. (2016), Mocz et al. (2017)), which result in similar, extended density profiles as calculated in the previous section. However, since this regime is not the focus of this thesis, this section will not provide calculations as thorough as before and the reader is referred to the references therein, as well as a recent review on the topic by Hui et al. (2017).

Here, the self-interaction pressure in equation (2.12) vanishes and the res-

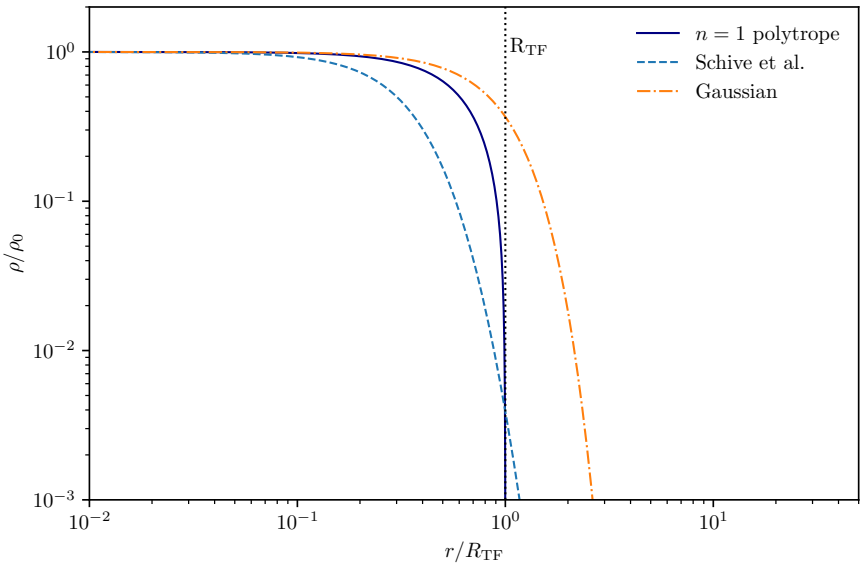

Figure 2.6: Density profiles for the fuzzy regime obtained from the analytic expressions in equations (2.28) and (2.30). They are compared to the $(n = 1)$-polytrope of the Thomas-Fermi regime. For all three cases $R_{\rm TF}$ is used as core (or scale) radius.

ulting equation reads

$$\nabla Q = -\nabla \Phi. \tag{2.27}$$

This equation gives rise to the solitonic cores - stable, minimum-energy solutions for self-gravitating FDM haloes - with constant central density, comparable to the cores in the Thomas-Fermi regime, hence also being a viable option to solve the small-scale problems. However, eq. (2.27) poses an eigenvalue problem and an exact solution can only be obtained numerically (see, e.g., Chavanis (2019)). Nevertheless, over the years several analytical approximations for the density profiles have been published, of which two are shown in Figure 2.6. Schive et al. (2014) introduced a density profile of the form[3]

$$\rho(r) = \frac{\rho_0}{\left[1 + (r/r_s)^2\right]^8}, \tag{2.28}$$

with central density ρ_0 and scale radius r_s. Furthermore, these solitonic cores are embedded in a NFW-like host halo, with a core-halo mass relation

$$M_c \propto a^{-1/2} M_{200}^{1/3}, \tag{2.29}$$

which depends on the redshift; here $a(t)$ describes the cosmic scale factor.

[3]The original work included a factor of 0.091 in the denominator. However, this factor can also be accounted for in the scale radius r_s.

Another approximation is given by the Gaussian profile,

$$\rho(r) = \rho_0 \exp\left(-\frac{r^2}{r_s^2}\right), \tag{2.30}$$

where the notation from Chavanis (2019) is used[4]. Figure 2.6 shows both profiles compared to a $(n = 1)$-polytrope with R_{TF} as scale radius for all three cases. Evidently, both profiles resemble the inner regions of the cored polytrope profile with constant central density. However, the density decrease around the core radius happens earlier for eq. (2.28) and is not as abrupt as for the $(n = 1)$-polytrope or the Gaussian profile. Moreover, Chavanis (2019) and Schobesberger et al. (2021) have shown that the $(n = 2)$-polytrope is another good fit, provided that the polytropic constant reads

$$K = \sqrt{\frac{2\pi G\hbar^2}{9m^2}}.$$

The density profile is then given by

$$\rho(r) = \rho_0 \theta(\xi)^2, \quad \xi = r\left(\frac{\hbar^2}{8\pi G m^2 \rho_0}\right)^{-1/4},$$

with $\theta(\xi)$ as the solution to the Lane-Emden equation for $n = 2$, which needs to be solved numerically.

[4]Others, like Schobesberger et al. (2021), used the factor 2σ instead of the scale radius r_s, where σ is the standard deviation of the distribution.

Chapter 3

Quantum-Hamilton-Jacobi framework

Another important and useful formulation for BEC dark matter haloes is given by the Quantum-Hamilton-Jacobi equation (QHJE). It is an equivalent description to the GP equation (2.1) and the quantum-hydrodynamic Euler equation (2.11). Based on the calculation of the latter, it is an easy task to set up an equation for the Hamiltonian of the system. This is accomplished through division of the real part of equation (2.6) by $|\psi|$, leading to

$$-\frac{\partial S}{\partial t} + \frac{\hbar^2}{2m}\frac{1}{|\psi|}\Delta|\psi| - \frac{1}{2m}(\nabla S)^2 - m\Phi - g|\psi|^2 = 0.$$

Making use of the definitions for the quantum potential (2.10) and bulk velocity (2.8), this equation can be rewritten as

$$-\frac{\partial S}{\partial t} = \frac{m\mathbf{v}^2}{2} + mQ + m\Phi + \frac{g\rho}{m} = \mathcal{H}, \tag{3.1}$$

which represents the total energy of the BEC halo. Here, the action function $S(\mathbf{r}, t)$ takes the place of a so-called generating function[1]; the goal of setting up a (Quantum-)Hamilton-Jacobi equation is to determine this function.

Although two limiting cases have been introduced in the previous chapter, the calculation of this generating function shall be done in the most general way, thus including quantum potential as well as self-interactions. Based on the Hamiltonian, the subsequent section then provides numerical results for the Thomas-Fermi regime.

3.1 Action-angle variables for SFDM

Before calculating the QHJE it is necessary to define the underlying framework of the method. The Hamiltonian in equation (3.1) will be used in spherical

[1] In Hamiltonian mechanics there are, in general, four different generating functions. Their name owes to the fact that their derivatives generate differential equations that determine the dynamics of the system in question.

coordinates (r, ϑ, φ). Furthermore, canonical transformations to more suitable, generalized coordinates will be made - the so-called action-angle variables. These action-angle variables generally arise from Hamilton-Jacobi equations and are especially useful when the latter are completely separable. To calculate the QHJE of the system it is of benefit to use momentum instead of velocity, hence equation (3.1) translates to[2]

$$\frac{\mathbf{p^2}}{2m} + mQ(r) + m\Phi(r) + \frac{g\rho(r)}{m} = -\frac{\partial S(\mathbf{r}, t)}{\partial t}. \tag{3.2}$$

The left-hand side of this equation, the Hamiltonian, can then be written as

$$\begin{aligned}\mathcal{H}(\mathbf{r}, \mathbf{p}, t) &= \frac{\mathbf{p^2}}{2m} + mQ + m\Phi + \frac{g\rho}{m} \\ &= \frac{1}{2m}\left(p_r^2 + \frac{p_\vartheta^2}{r^2} + \frac{p_\varphi^2}{r^2 \sin^2 \vartheta}\right) + mQ + m\Phi + \frac{g\rho}{m},\end{aligned} \tag{3.3}$$

or, as it will be used later, in matrix notation,

$$\begin{aligned}\mathcal{H}(\mathbf{r}, \mathbf{p}, t) = \begin{pmatrix} p_r & p_\vartheta & p_\varphi \end{pmatrix} \begin{pmatrix} 1/m & 0 & 0 \\ 0 & 1/mr^2 & 0 \\ 0 & 0 & 1/mr^2 \sin^2 \vartheta \end{pmatrix} \begin{pmatrix} p_r \\ p_\vartheta \\ p_\varphi \end{pmatrix} \\ + mQ + m\Phi + \frac{g\rho}{m}.\end{aligned} \tag{3.4}$$

In this context the generating function S is called *Hamilton's principle function.* Its key role is to enable the canonical transformations

$$\mathbf{p} = \frac{\partial S(\mathbf{r}, t)}{\partial \mathbf{r}} \qquad \Rightarrow \qquad p_r = \frac{\partial S}{\partial r}, \quad p_\vartheta = \frac{\partial S}{\partial \vartheta}, \quad p_\varphi = \frac{\partial S}{\partial \varphi},$$

which, after inserting these expressions into the Hamiltonian in eq. (3.2), effectively yields a new Hamiltonian $\mathcal{K}$,

$$\begin{aligned}\mathcal{K}\left(\mathbf{r}, \frac{\partial S}{\partial \mathbf{r}}, t\right) = \frac{1}{2m}\left(\frac{\partial S}{\partial r}\right)^2 + mQ + m\Phi + \frac{g\rho}{m} + \frac{1}{2mr^2}\left(\frac{\partial S}{\partial \vartheta}\right)^2 \\ + \frac{1}{2mr^2 \sin^2 \vartheta}\left(\frac{\partial S}{\partial \varphi}\right)^2 + \frac{\partial S}{\partial t} = 0.\end{aligned} \tag{3.5}$$

This equation is the desired Hamilton-Jacobi equation. Due to the quantum potential Q appearing in it, this form is often more precisely referred to as *Quantum-Hamilton-Jacobi equation* (Wyatt, 2005). Its main advantage is that, since it is zero, the generalized coordinates, as well as the canonically conjugated momenta, are constants and thus conserved quantities. However,

[2]Since spherical symmetry is assumed for the density ρ, the same is done for quantum potential Q and gravitational potential Φ; hence the dependence on r only.

solving this partial differential equation is not trivial and is usually only done when separation of variables can be applied to Hamilton's principle function. Whether the Hamilton-Jacobi equation separates depends on both the physical problem and the chosen coordinate system[3]. Although there is no general way of finding out if separability is feasible, conveniently for orthogonal coordinate systems there are the so-called *Stäckel conditions* (developed by Stäckel (1891), see also Goldstein et al. (2001), Boccaletti and Pucacco (2004)) in order to determine if separation is possible. These five conditions read:

1. The Hamiltonian is conserved.
2. The Hamiltonian can be written in the form
$$\mathcal{H} = \frac{1}{2}\left(\mathbf{p}^\top - \mathbf{a}^\top\right)\mathcal{T}^{-1}(\mathbf{p} - \mathbf{a}) + V(q) \tag{3.6}$$
with the vector $\mathbf{a}$ depending linearly on the generalized momenta and a square matrix $\mathcal{T}$, whose elements depend on the chosen coordinate system.
3. The elements of vector $\mathbf{a}$ only depend on the corresponding coordinate, i.e. $a_i = a_i(q_i)$.
4. The potential can be written in the form
$$V(q) = \sum_i \frac{V_i(q_i)}{\mathcal{T}_{ii}}. \tag{3.7}$$
5. There exists a matrix ϕ with an inverse ϕ^{-1}, where the diagonal elements of both matrices only depend on the corresponding coordinate or are constants. According to Greenwood (1997), the elements of ϕ can be determined through
$$\phi_{ij} = \frac{\partial W_i}{\partial q_i}\frac{\partial^2 W_i}{\partial q_i \partial \alpha_j}. \tag{3.8}$$

Hereafter, the Stäckel conditions shall be worked out in order to verify if this solution approach can be applied to our system.

First, whenever a Hamilton-Jacobi equation does not depend explicitly on time, the principle function can be written in the form
$$S(\mathbf{r}, t) = W(\mathbf{r}) - \alpha_t t, \tag{3.9}$$

[3]For example, the Kepler problem can be separated in plane polar coordinates (r, ϕ), but not in Cartesian coordinates (x, y, z).

with W now called *Hamilton's characteristic function* and an integration constant α_t. This poses the question whether the same procedure can be applied again, and if, under which circumstances? We are therefore looking for a solution that reads

$$W = W_j(q_j, \alpha) + W'(q_i, \alpha),$$

where W' depends on all generalized coordinates q_i except q_j, and where α represents some constant. Whenever this is the case, the Hamilton-Jacobi equation takes the form

$$\mathcal{H}\left(q_i, \frac{\partial W'}{\partial q_i}, f\left(q_j, \frac{\partial W_j}{\partial q_j}\right)\right) = \alpha_1, \tag{3.10}$$

with α_1 representing a constant. The equation can then be inverted and solved for the function f, leading to

$$f\left(q_j, \frac{\partial W_j}{\partial q_j}\right) = g\left(q_i, \frac{\partial W'}{\partial q_i}, \alpha_1\right).$$

Since the left-hand side of this equation depends only on the coordinates q_j, whereas the right-hand side depends on the other q_i, it can exclusively be satisfied when both sides are equal to the same constant. The equation can thus be written as

$$f\left(q_j, \frac{\partial W_j}{\partial q_j}\right) = \alpha_j = g\left(q_i, \frac{\partial W'}{\partial q_i}\right)$$

and another potential variable separation has been carried out. To continue with the Stäckel conditions, it is evident that inserting equation (3.9) into the QHJE (3.5) yields

$$\mathcal{H} = \alpha_t = E,$$

the constant α_t is thus identified as the total energy of the system. Furthermore, the Hamiltonian is conserved and the first Stäckel condition is automatically satisfied. The Quantum-Hamilton-Jacobi equation then reads

$$\frac{1}{2m}\left(\frac{\partial W}{\partial r}\right)^2 + mQ + m\Phi + \frac{g\rho}{m} + \frac{1}{2mr^2}\left(\frac{\partial W}{\partial \vartheta}\right)^2 + \frac{1}{2mr^2\sin^2\vartheta}\left(\frac{\partial W}{\partial \varphi}\right)^2 = E. \tag{3.11}$$

For the second condition a comparison between the expressions (3.4) and (3.6) reveals that $\mathbf{a} = \mathbf{0}$ in this system. Moreover, the 3×3 matrix $\mathcal{T}^{-1}$ can be identified as

$$\mathcal{T}^{-1} = \begin{pmatrix} 1/m & 0 & 0 \\ 0 & 1/mr^2 & 0 \\ 0 & 0 & 1/mr^2\sin^2\vartheta \end{pmatrix},$$

with its inverse

$$\mathcal{T} = \begin{pmatrix} m & 0 & 0 \\ 0 & mr^2 & 0 \\ 0 & 0 & mr^2 \sin^2 \vartheta \end{pmatrix}.$$

Now, the potential $V(q)$ is the sum of gravitational potential, quantum potential and the self-interaction term,

$$V(q) = V(r) = m\Phi(r) + mQ(r) + \frac{g\rho(r)}{m}, \tag{3.12}$$

and therefore the second condition is met. Since the Hamiltonian does not depend linearly on the generalized momenta and thus $\mathbf{a} = \mathbf{0}$, condition three is again automatically satisfied. The fourth Stäckel condition also imposes constraints on the potential. From eq. (3.7) one can see that the most general form of a potential for a single-particle system can be written as

$$V(q) = V_r(r) + \frac{V_\vartheta(\vartheta)}{r^2} + \frac{V_\varphi(\varphi)}{r^2 \sin^2 \vartheta}.$$

Given that spherical symmetry is assumed and thus $V_\vartheta(\vartheta) = V_\varphi(\varphi) = 0$, the equation reduces exactly to eq. (3.12), hence this condition is fulfilled. Finally, the arguably most bewildering condition demands the existence of the matrices ϕ and ϕ^{-1}. Equation (3.8) is used to determine the elements of ϕ, and then obtain the elements of ϕ^{-1} by simply performing matrix inversion. This can be accomplished by assuming a separation approach for Hamilton's characteristic function, i.e.

$$W(\mathbf{r}) = W(r, \vartheta, \varphi) = W_r(r) + W_\vartheta(\vartheta) + W_\varphi(\varphi).$$

Evidently, when inserting this expression into equation (3.11), it does not depend explicitly on the coordinate φ; φ is therefore a cyclic coordinate. When this is the case,

$$p_\varphi = \frac{\partial W_\varphi}{\partial \varphi} = \alpha_\varphi, \tag{3.13}$$

with α_φ being another integration constant (just like α_t earlier). With this result the remaining equation reads

$$\frac{1}{2m}\left(\frac{\partial W_r}{\partial r}\right)^2 + mQ + m\Phi + \frac{g\rho}{m} + \frac{1}{2mr^2}\left[\left(\frac{\partial W_\vartheta}{\partial \vartheta}\right)^2 + \frac{\alpha_\varphi^2}{\sin^2 \vartheta}\right] = E. \tag{3.14}$$

Only the terms in square brackets of equation (3.14) depend upon the coordinate ϑ (and only upon ϑ). Thus, the Hamiltonian takes exactly the form of eq. (3.10) and it can be inferred that these terms must be constant as well,

$$\left(\frac{\partial W_\vartheta}{\partial \vartheta}\right)^2 + \frac{\alpha_\varphi^2}{\sin^2 \vartheta} = \alpha_\vartheta^2, \tag{3.15}$$

from which follows that

$$p_\vartheta = \frac{\partial W_\vartheta}{\partial \vartheta} = \sqrt{\alpha_\vartheta^2 - \frac{\alpha_\varphi^2}{\sin^2 \vartheta}}.$$

Inserting this expression into eq. (3.14) yields

$$\left(\frac{\partial W_r}{\partial r}\right)^2 + \frac{\alpha_\vartheta^2}{r^2} = 2m\left(E - m\Phi - mQ - \frac{g\rho}{m}\right),$$

which solely depends on the coordinate r and allows for the momentum to be calculated,

$$p_r = \frac{\partial W_r}{\partial r} = \sqrt{2m\left(E - m\Phi - mQ - \frac{g\rho}{m}\right) - \frac{\alpha_\vartheta^2}{r^2}}.$$

Finally, the matrix ϕ can be constructed by using equation (3.8). Their individual elements read

$$\phi_{11} = \frac{\partial W_r}{\partial r}\frac{\partial^2 W_r}{\partial r \partial \alpha_t} = m \quad \phi_{12} = \frac{\partial W_r}{\partial r}\frac{\partial^2 W_r}{\partial r \partial \alpha_\vartheta} = -\frac{\alpha_\vartheta}{r^2} \quad \phi_{13} = \frac{\partial W_r}{\partial r}\frac{\partial^2 W_r}{\partial r \partial \alpha_\varphi} = 0$$

$$\phi_{21} = \frac{\partial W_\vartheta}{\partial \vartheta}\frac{\partial^2 W_\vartheta}{\partial \vartheta \partial \alpha_t} = 0 \quad \phi_{22} = \frac{\partial W_\vartheta}{\partial \vartheta}\frac{\partial^2 W_\vartheta}{\partial \vartheta \partial \alpha_\vartheta} = \alpha_\vartheta \quad \phi_{23} = \frac{\partial W_\vartheta}{\partial \vartheta}\frac{\partial^2 W_\vartheta}{\partial \vartheta \partial \alpha_\varphi} = \frac{-\alpha_\varphi}{\sin^2 \vartheta}$$

$$\phi_{31} = \frac{\partial W_\varphi}{\partial \varphi}\frac{\partial^2 W_\varphi}{\partial \varphi \partial \alpha_t} = 0 \quad \phi_{32} = \frac{\partial W_\varphi}{\partial \varphi}\frac{\partial^2 W_\varphi}{\partial \varphi \partial \alpha_\vartheta} = 0 \quad \phi_{33} = \frac{\partial W_\varphi}{\partial \varphi}\frac{\partial^2 W_\varphi}{\partial \varphi \partial \alpha_\varphi} = \alpha_\varphi,$$

which gives ϕ as

$$\phi = \begin{pmatrix} m & -\alpha_\vartheta/r^2 & 0 \\ 0 & \alpha_\vartheta & -\alpha_\varphi/\sin^2 \vartheta \\ 0 & 0 & \alpha_\varphi \end{pmatrix}$$

and its inverse ϕ^{-1} as

$$\phi^{-1} = \begin{pmatrix} 1/m & 1/mr^2 & 1/mr^2 \sin^2 \vartheta \\ 0 & 1/\alpha_\vartheta & 1/\alpha_\varphi \sin^2 \vartheta \\ 0 & 0 & 1/\alpha_\varphi \end{pmatrix}.$$

The diagonal elements of both matrices depend only on constants and thus the fifth Stäckel condition is satisfied. The Quantum-Hamilton-Jacobi equation (3.5) is therefore completely separable.

Before proceeding with the calculation of action-angle variables, it is helpful to take a closer look at the integration constants α_φ and α_ϑ emerging here. From equation (3.13), the former can be identified as the angular momentum component in z-direction, $\alpha_\varphi = L_z$, as described in Binney and Tremaine (2008). Furthermore, when rewriting eq. (3.15) as

$$p_\vartheta^2 + \frac{p_\varphi^2}{\sin^2 \vartheta} = \alpha_\vartheta^2,$$

one can see that $\alpha_\vartheta = |\mathbf{L}| = L$ is the magnitude of the angular momentum vector. Thus, together with the constant $\alpha_t = E$, these three constants represent the conservation of energy, of the magnitude of angular momentum and of its component L_z. With this knowledge Hamilton's principle function S can now be fully expressed and takes the form

$$\begin{aligned} S(\mathbf{r},t) &= W(\mathbf{r}) - Et = W_r(r) + W_\vartheta(\vartheta) + W_\varphi(\varphi) - Et \\ &= \int \mathrm{d}r \sqrt{2m\left(E - m\Phi - mQ - \frac{g\rho}{m}\right) - \frac{L^2}{r^2}} + \int \mathrm{d}\vartheta \sqrt{L^2 - \frac{L_z^2}{\sin^2\vartheta}} \\ &\quad + \int \mathrm{d}\varphi L_z - Et. \end{aligned}$$

Finally, the last task is to calculate the action-angle variables. The generalized momenta, the actions, are defined as

$$J_i = \frac{1}{2\pi} \oint p_i \mathrm{d}q_i = \frac{1}{2\pi} \oint \frac{\partial S_{q_i}}{\partial q_i} \mathrm{d}q_i, \tag{3.16}$$

with the old coordinates q_i and momenta p_i, while the respective coordinates, called angles, can be calculated by

$$\dot{\theta}_i = \frac{\partial \mathcal{H}}{\partial J_i} = \Omega_i. \tag{3.17}$$

This new set of variables defines an invariant three-torus, as schematically depicted in Figure 3.1 for two dimensions, with the actions J_r, J_ϑ and their corresponding angles $\Omega_r, \Omega_\vartheta$. The resulting action integrals for spherical SFDM haloes read

$$J_\varphi = \frac{1}{2\pi} \int \mathrm{d}\varphi L_z = L_z, \tag{3.18}$$

$$J_\vartheta = \frac{1}{2\pi} \int \mathrm{d}\vartheta \sqrt{L^2 - \frac{L_z^2}{\sin^2\vartheta}}, \tag{3.19}$$

$$J_r = \frac{1}{2\pi} \int \mathrm{d}r \sqrt{2m\left(E - m\Phi - mQ - \frac{g\rho}{m}\right) - \frac{L^2}{r^2}}. \tag{3.20}$$

Computing these actions analytically is only possible for few cases, even if the quantum potential and self-interaction are disregarded. One special case is the isochrone potential (Henon (1959a), Henon (1959b)) which includes the homogeneous sphere and Kepler potential as limiting cases. A derivation of the analytical solutions of this particular potential is given in Appendix A.

3.2 Orbits in the Thomas-Fermi regime

With the actions calculated for SFDM, it is now possible to investigate them further in the Thomas-Fermi approximation. While equations (3.18) and (3.19)

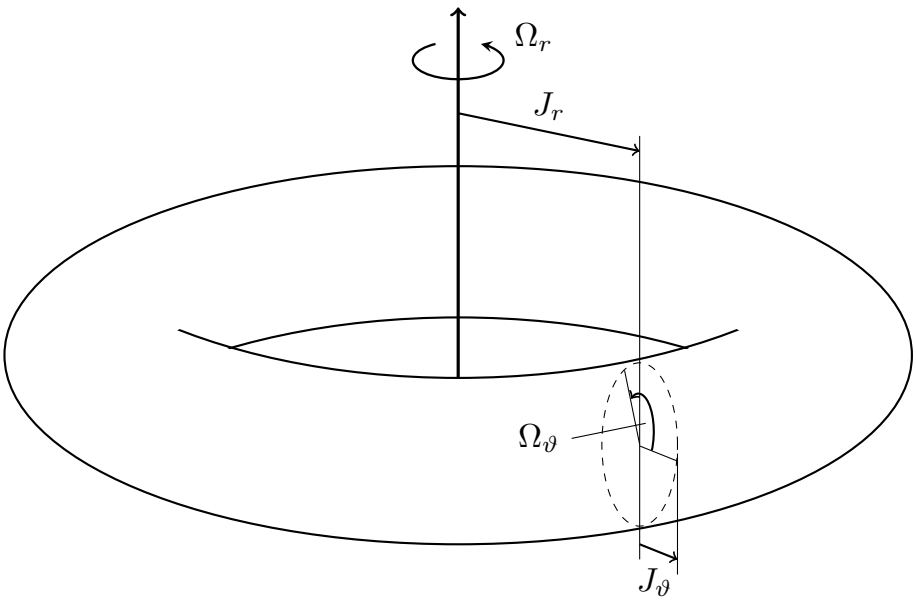

Figure 3.1: Invariant two-torus for a two-dimensional potential. The actions J_r and J_ϑ define the size of the torus, while the angles Ω_r and Ω_ϑ define the particle position, i.e. its trajectory on the torus. Note that both angles repeat periodically with 2π.

do not change in this regime, the radial action (3.20) gets simplified by dropping the Q-term and thus reads

$$J_r = \frac{1}{2\pi} \int \mathrm{d}r \sqrt{2m \left(E - m\Phi - \frac{g\rho}{m} \right) - \frac{L^2}{r^2}}.$$

The complete expression is then given when inserting the gravitational potential of the TF regime (2.19) into this equation.

To visualize the constant actions, a numerical calculation is required. The Python package of choice to accomplish this is `gala`[4], developed for performing common tasks associated with galactic dynamics[5] (Price-Whelan, 2017). `gala` allows to define miscellaneous potentials, if not pre-defined already, and is able to calculate stellar (or, in this case, dark matter particle) orbits and their corresponding action-angle variables. While orbit integration is implemented straightforward and can be done with multiple integrators (e.g. the Dormand-Prince method, Leapfrog integration, fifth-order Runge-Kutta, and others), the transformation to action-angles is based on work by Sanders and Binney (2014). The formalism described therein relies on torus mapping, a method which provides orbits with specified actions instead of orbits with specified initial conditions. This way it is possible to derive actions and angles (and thus frequencies) for a series of phase-space coordinates (x_i, v_i), evolved along an orbit for several timesteps $0 \leq t_i \leq T$, where T specifies the total time

[4] http://gala.adrian.pw/en/latest/

[5] Another available module would be `galpy` (Bovy, 2015). However, this package only allows orbit integration for already defined potentials; the $(n = 1)$-polytrope potential is not included.

span for integration. With this series it is possible to create a generating function that maps a toy torus of a simple toy potential into the desired torus describing the particle's orbit. These toy potentials can be divided into two categories: A triaxial harmonic oscillator is used for box orbits, while loop orbits are described by the isochrone potential. As the $(n = 1)$-polytrope potential considered here is part of the latter family, the isochrone potential is the toy potential of choice[6].

With the potential defined and the Hamiltonian of the Thomas-Fermi regime,

$$\mathcal{H} = \frac{1}{2m}\left(p_r^2 + \frac{p_\vartheta^2}{r^2} + \frac{p_\varphi^2}{r^2 \sin^2 \vartheta}\right) + m\Phi + \frac{g\rho}{m},$$

implemented, `gala` integrates the orbit for a number of specified timesteps and calculates from them the actions and angles. Figure 3.2 visualizes the derived orbits in the Thomas-Fermi core-region of a BEC halo in Cartesian coordinates (x, y, z) with arbitrarily chosen initial conditions of $[1, 1, 0]$ kpc for the positions, $[0, 50, 30]$ km s^{-1} for the particle velocities and a total of 4000 timesteps, which translate to 2 Gyr. It is important to note that, for realistic particle positions and velocities, the gravitational potential enables (almost) circular orbits, which is an important underlying assumption in Chapter 4.

Furthermore, the associated actions J_r, J_ϑ and J_φ are presented in Figure 3.3. Evidently, all three actions show almost constant behaviour, with variations only in the range of 10^{-10}. Shorter integration times reveal a minor sinusoidal superimposition in all three actions. Although this does not affect the overall "constant" nature of the actions, it might stem from the choice of gravitational potential - the sinus in equation (2.19).

[6]Generally speaking, box orbits are observed in triaxial systems, while loop orbits occur in systems with spherical or axisymmetric symmetry.

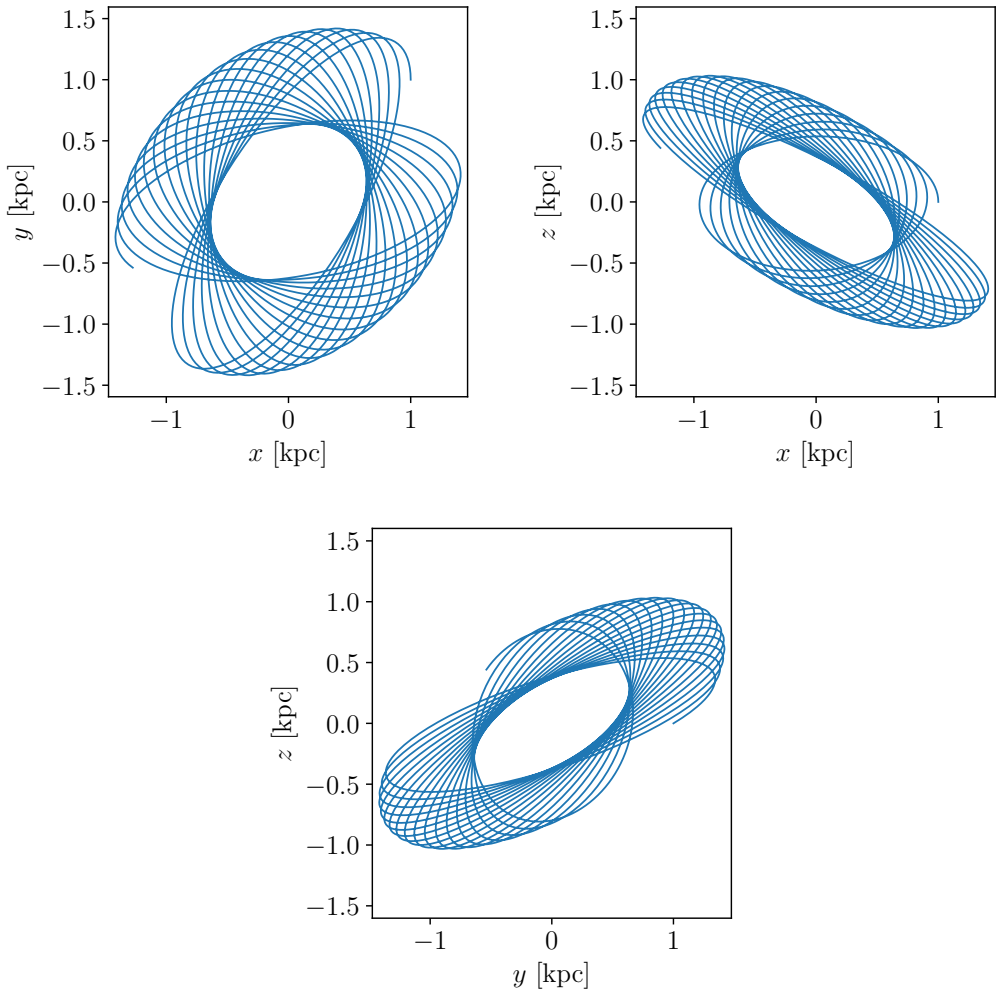

Figure 3.2: Particle orbits in Cartesian coordinates (x, y, z) for a SFDM halo in the self-interacting Thomas-Fermi regime with core radius $R_{\mathrm{TF}} = 4$ kpc obtained with `gala`. The initial conditions were chosen arbitrarily as $x_i \in [1, 1, 0]$ kpc for positions and $v_i \in [0, 50, 30]$ km s^{-1} for velocities.

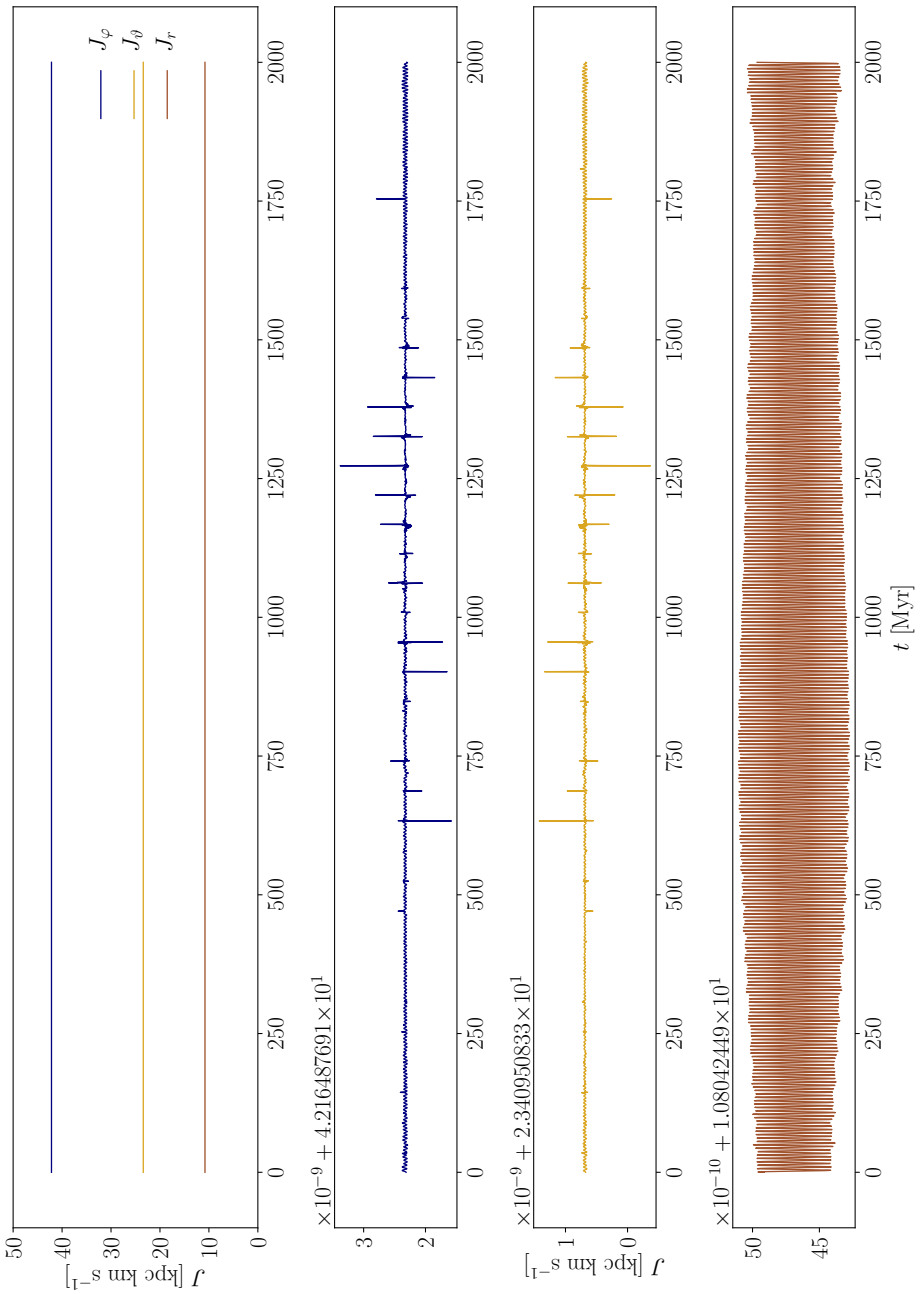

Figure 3.3: Corresponding actions J_i for the orbits in Figure 3.2. The *top* panel shows all three actions plotted together; the variations are so small that, at this scale, the graphs look completely constant. The *bottom* three panels show zoomed-in versions for J_φ, J_ϑ and J_r, respectively. For each of the panels the numbers on the upper left corner indicate a base and an offset. Only at these scales the variations are clearly visible. This stability thus enables the actions to create the surface of a three-dimensional invariant torus as depicted in Figure 3.1 for two dimensions.

Chapter 4

Adiabatic contraction

Chapters 2 and 3 were dedicated to the calculation of several physical quantities associated with Bose-Einstein condensed SFDM haloes. However, these calculations were performed while neglecting the presence of baryonic matter and thus were focused solely on the dark matter component. This chapter will present a model to study the gravitational response of dark matter particles due to baryonic accumulations in the center of haloes, applied to SFDM. When gravitational potentials undergo slow variations compared to the typical orbital frequency, these changes are called adiabatic and their associated action integrals $\int p\mathrm{d}q$, as calculated in equations (3.18) - (3.20), remain constant during the variation. These actions are therefore often referred to as adiabatic invariants, while the model is suitably called adiabatic contraction (AC), referring to the inward pull of dark matter due to baryons.

Among the first to consider these adiabatic invariants in order to gain information about the dynamics in contracting galaxies were Eggen et al. (1962). In the context of planetary orbits around a star, they calculated the radial action in an isochrone potential, equation (A.10), as presented in Appendix A. Zel'dovich et al. (1980) later used the approach of collapsing matter dragging weakly interacting leptons inwards to infer mass bounds of these heavy, stable and neutral leptons, which ultimately led to the preclusion of such leptons to account for the missing mass in galaxies and clusters. Then, a few years later, Barnes and White (1984) further used this model in a collisionless N-body code to determine the response of a proto-bulge to the gravitational influence of an exponential disk located in the center of the bulge. However, the most influential publications on this topic are Blumenthal et al. (1986), who first named it adiabatic contraction, and Ryden and Gunn (1987), whose studies were carried out concurrently. While the former presented the analytic framework for the adiabatic invariants of dissipationless particle orbits specifically for galactic haloes with an emphasis on the Milky Way, the latter embedded the theory on a much larger scale, starting from small perturbations in the initial density of a CDM Universe, which served as seeds for subsequent contraction. Both studies, however, were able to create flat rotation curves

as observed in the Universe, effectively achieved through the gravitational contraction due to infalling baryons.

Following Blumenthal et al. (1986), we can exploit the discussed properties of adiabatic invariants. For the basic presumption that a dark matter particle moves along a circular orbit at radius r inside a spherically symmetric mass distribution $M(r)$, the quantity $rM(r)$ remains constant. This expression represents the squared angular momentum in spherical potentials, occuring in equations (3.18), (3.19) and (3.20) for the actions. Equations (3.18) and (3.19) can be evaluated readily, just like equations (A.3) and (A.4), see Appendix A. The condition $L^2 = rM(r) = \text{const.}$ can then be used to calculate the response of dark matter particles to baryonic particles inside a halo, where the fraction of baryonic matter is determined by $f = M_b(r_f)/M_{\text{tot}}$. Given an initially spherically symmetric mass distribution $M_i(r_i)$, the baryons inside such a halo fall inwards onto a final baryonic mass distribution $M_b(r_f)$, dragging with them the surrounding dark matter particles. From the particle orbits' adiabatic invariant one can then deduce

$$r_f \left[M_{\text{dm}}(r_f) + M_b(r_f)\right] = r_i M_i(r_i) = r_i \frac{M_{\text{dm}}(r_f)}{1-f}, \tag{4.1}$$

where $M_{\text{dm}}(r_f)$ describes the dark matter mass profile after contraction. Equation (4.1) needs to be solved iteratively for $M_{\text{dm}}(r_f)$ in order to remain constant. To study the contraction, Blumenthal et al. (1986) assumed a pseudo-isothermal sphere as initial distribution for the (dissipationless) dark matter component, whose mass profile is described by

$$M_{\text{pis}}(r) = \frac{4\pi\rho_0 r_h^2}{9}\left(3r - \sqrt{3}r_h \arctan\left[\frac{\sqrt{3}r}{r_h}\right]\right), \tag{4.2}$$

with central density ρ_0 and core radius r_h, which they chose to be 42% of the outer halo radius. Combined with the baryonic mass distribution of an exponential disk,

$$M_b(r) \propto 1 - \left(1 + \frac{r}{b}\right)\exp\left(-\frac{r}{b}\right), \tag{4.3}$$

where b represents the associated scale length, they investigated contractions for various configurations, i.e. high or low baryon fractions, and a small or large exponential disk. Their considerations provided an opportunity to verify the correctness of the Python code written for this method[1], which is shown in Appendix B, and effectively made it possible to recreate Figure 1 and 2 of the original publication. The velocity profiles in Figure 4.1 best show the response of the dark matter particles to the embedded exponential disk; e.g.

[1]The core concept of the code, the contraction based on equation (4.1), was taken from the implementation by Freese et al. (2009). Although applied there on a much smaller scale, namely that of dark stars, the iterative process to solve the equation is identical. Some alterations had to be implemented to fit the environment considered for our purpose.

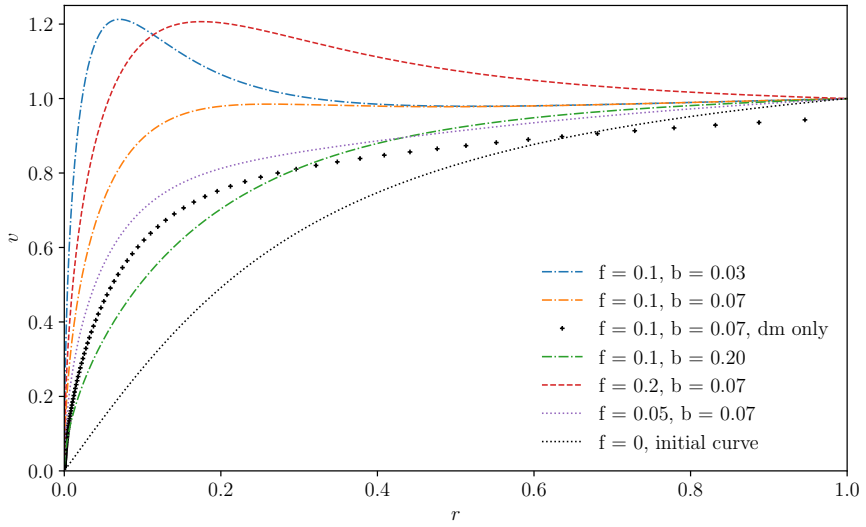

Figure 4.1: Circular velocities based on equation (1.1) for several baryon fractions f and scale lengths b of the baryon mass profile in equation (4.3), with normalization such that $v(1) = 1$. These results are obtained from the adiabatic invariant condition in equation (4.1) and show the effect baryons have on the initial, underlying dark matter mass profile in eq. (4.2) (black dotted line). This plot may be compared to Figure 1 in Blumenthal et al. (1986).

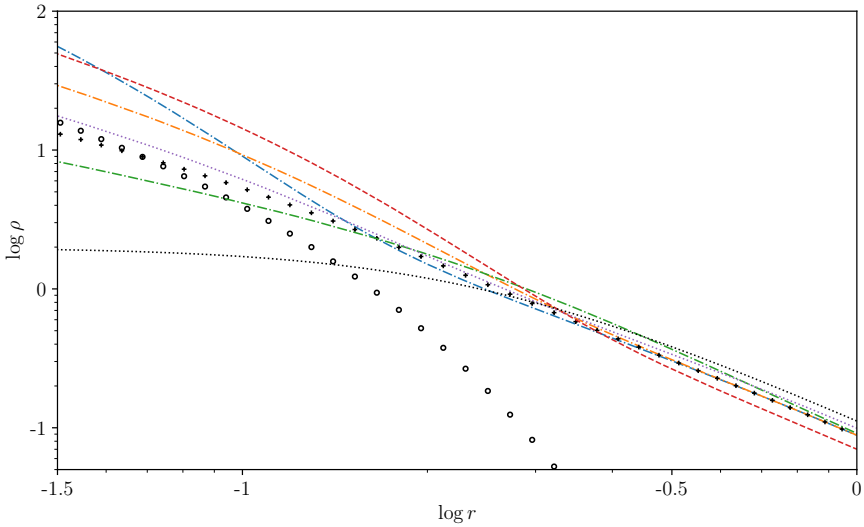

Figure 4.2: Corresponding densities ρ to the velocities in Figure 4.1, with identical cases shown. Additionally, the open circles show the baryonic density profile for $f = 0.1$ and $b = 0.07$. As in Blumenthal et al. (1986), the density is normalized such that $M(1) = 1$. This plot may be compared to Figure 2 in Blumenthal et al. (1986).

the blue dot-dashed line, which describes a small baryonic disk concentrated in the center of the halo, leads to a sharp peak in the inner regions of the halo, while the green dot-dashed line shows a more outspread disk, resulting in significantly less qualitative changes of the velocity profile. This can be further seen in Figure 4.2 for the density profiles, where the slope of the final curve for the case of $f = 0.1$, $b = 0.07$ (orange dot-dashed line) increases slightly in the regions where the baryonic density (open circles) gets significant enough. The central density of this case thus rises by more than one order of magnitude.

Although this adiabatic contraction model has been used extensively to calculate the effect of baryons on dark matter particles in haloes, its assumption of purely circular orbits is merely an approximation. This led Gnedin et al. (2004) to publish a modification of the model that accounts for highly eccentric orbits. This is achieved through the usage of an orbit-averaged radius $\bar{r}$ that is defined as

$$\bar{r} = Ar^w,$$

with halo-to-halo variations of the parameters A and w. With mean values of $A \approx 0.85 \pm 0.05$ and $w \approx 0.8 \pm 0.02$, the conserved quantity of the Blumenthal model is adjusted such that $rM(\bar{r})$ is constant instead. This modification further resolves the general overprediction of the contraction of the Blumenthal method in the inner parts of haloes, $r/r_{\mathrm{vir}} \lesssim 0.1$, where r_{vir} is the virial radius of the halo (see, e.g., Duffy et al. (2010), Cautun et al. (2020)). Compared to high-resolution cosmological simulations, the modified model results in deviations of only $\lesssim 10\%$, while also avoiding systematic over- and underpredictions of the resulting density.

Furthermore, Cautun et al. (2020) recently studied the mass profile of the Milky Way as inferred from fitting models to the galactic rotation curve with Gaia data. They argued that adiabatic contraction models have rarely been used in the context of the Milky Way, and that the contraction is mostly ignored. However, omitting the change in the dark matter density, which plays a crucial role in determining its mass profile, leads to systematic biases, especially in the central parts of the Galaxy. This provides a motivation for the study of adiabatic contraction, even more so because it has thus far not been tested in SFDM cosmologies.

4.1 Adiabatic contraction in the Thomas-Fermi regime

Using the results of the previous sections, we can study now the gravitational contraction of SFDM haloes due to baryonic matter. In order to make comparisons to observables in the Universe and to previous literature as straightforwardly as possible, various parameters have to be chosen accordingly.

- **Initial dark matter profile** Since the goal is to study haloes in the Thomas-Fermi regime and in the presence of baryons, the profile of choice

is that obtained in Section 2.3, i.e. an $(n = 1)$-polytropic core surrounded by an isothermal envelope. Due to numerical instabilities of Method 1, it is favourable to use the differential equation (2.26) of Method 2 to calculate the density profile. With a realistic value of $\chi = 1$, the enclosed mass at each initial radius r_i can then be determined. In addition, core radii in the range of $R_{\mathrm{TF}} \in [0.1, 4]$ kpc are used.

- **Final baryon profile** With the small-scale problems of CDM in mind, it is especially interesting to study adiabatic contraction on the scale of dwarf galaxies. The Hernquist profile (Hernquist, 1990) has been used frequently in the literature to model the baryon component of dwarf galaxies, so it is applied here, as well. It allows for an analytic description of the baryon density profile and reads

$$\rho(r) = \frac{\rho_s}{\frac{r}{b}\left(1 + \frac{r}{b}\right)^3},$$

where ρ_s again is a reference density and b specifies the scale radius[2], and gives a good approximation for dwarf spheroidals. Although considering much smaller scales, we will follow Blumenthal et al. (1986) and test three scale lengths; $b = 0.03$ will describe a small spheroidal, $b = 0.07$ is used for the intermediate case and $b = 0.2$ accounts for a more extended galaxy.

- **Baryon fraction** This parameter can vary greatly, with some dwarf galaxies almost completely lacking dark matter and thus a baryon fraction of nearly unity (van Dokkum et al., 2018). However, such galaxies are rare and most dwarfs are highly dark-matter-dominated, in fact. Most literature uses fractions of the order of the cosmic mean, $f = 0.157$. Duffy et al. (2010) showed that baryonic feedback, e.g. due to AGN or supernovae, leads to a decrease of this value from $z = 2$ to $z = 0$. Given the uncertainties, we choose baryon fractions as $f = 0.07, 0.10, 0.13, 0.15$ in order to cover a wide range of parameters.

- **Halo parameters** Finally, it is possible to define the virial mass and radius of a dark matter halo in order to calculate the velocity dispersion,

$$\sigma^2 = \frac{GM_{200}}{R_{200}} = \text{const.},$$

where the subscript $_{200}$ indicates the radius at which the density is 200 times the critical density of the Universe, which translates approximately to the virial mass and radius. The constancy of the velocity dispersion effectively guarantees the pressure to be isothermal, as seen in equation (2.22), which is appropriate for the halo envelope in the Thomas-Fermi

[2]Although much of the literature uses r_s to describe the scale radius, Hernquist used the variable a, instead, in his original work. Moreover, in order to avoid confusion, it is important to note that in the code this scale radius is specified as b, as motivated by Blumenthal et al. (1986).

regime. However, sometimes it is favourable to define the central density ρ_0 instead, leading to the free choice of either $\{R_{\rm TF}, \sigma^2\}$ or $\{R_{\rm TF}, \rho_0\}$; this approach was also implemented in Dawoodbhoy et al. (2021).

So far, simulations including the baryonic component are rare for SFDM cosmologies. Unfortunately, the few simulations available in the literature are focused solely on FDM, while there are none for the Thomas-Fermi regime. Thus, in order to put our results into context, we proceed with a comparison to a recently published study by Mocz et al. (2020) for FDM. In this work they performed cosmological simulations of ultra-light bosons with mass $m = 2.5 \cdot 10^{-22}$ eV in the fuzzy regime[3], thus neglecting particle self-interactions. Starting from initial conditions, they simulate the evolution of a FDM Universe from $z = 63$ to $z = 5.5$, from which they identify three haloes with different mass, radius and baryon fractions. Focusing on the largest of FDM haloes, halo 1 with $M_{200} = 8.2 \cdot 10^9\, M_\odot$ and $R_{200} = 42$ kpc, they show its density profile for a run involving full baryon physics and one with dark matter only, see Figure 4 in Mocz et al. (2020). The implemented baryon physics includes supernova feedback through kinetic winds, primordial cooling, metal-line cooling to also account for heavier elements, and (stochastic) star formation. They further approximate reionization to occur uniformly and instantaneous at a redshift of $z \sim 6$. Although some small variations between the runs with and without baryons are visible at ~ 5 kpc h^{-1} (with h being the reduced Hubble constant, $h = H_0/100$), the profiles essentially follow the same decline, which is roughly proportional to r^{-2}. Based upon their equation (14), the soliton core radius of this halo at the redshift of $z = 6$ amounts to $x_c = 1$ kpc.

Figure 4.3 now shows the results of our calculations for the same halo in the Thomas-Fermi regime; the top panel displays velocities, the bottom panel shows densities. While our analysis is much more simplistic with regard to the baryon physics than that in Mocz et al. (2020), the considered adiabatic contraction model allows to resolve very small scales, i.e. the very halo centers, unlike cosmological simulations. In order to obtain similar central densities of $\rho_0 \sim 10^9 M_\odot$ kpc^{-3}, the Thomas-Fermi regime requires a core radius larger by a factor of at least four, thus $R_{\rm TF} \geq 4$ kpc, when compared to the FDM case. Furthermore, it is evident that the baryonic spheroidal in the core affects the dark matter particles in the envelope outside of $R_{\rm TF}$ (indicated by a vertical dotted line) comparatively little. This changes drastically from roughly 0.5 kpc inwards, where the baryons are concentrated. Here, they are able to compress the core further, leading to an increase in the dark matter density by more than two orders of magnitude. This increase then also leads to a boost in velocity at these radii. Although not shown, the cases $b = 0.03$ and $b = 0.2$ follow the same general trend but with slightly steeper or shallower density slopes in the core regions, respectively.

Robles et al. (2019) conducted a study of the fuzzy regime in the light of

[3]Note that, despite simulating only the FDM regime, they use the terms "fuzzy dark matter" and "Bose-Einstein-condensed dark matter" synonymously.

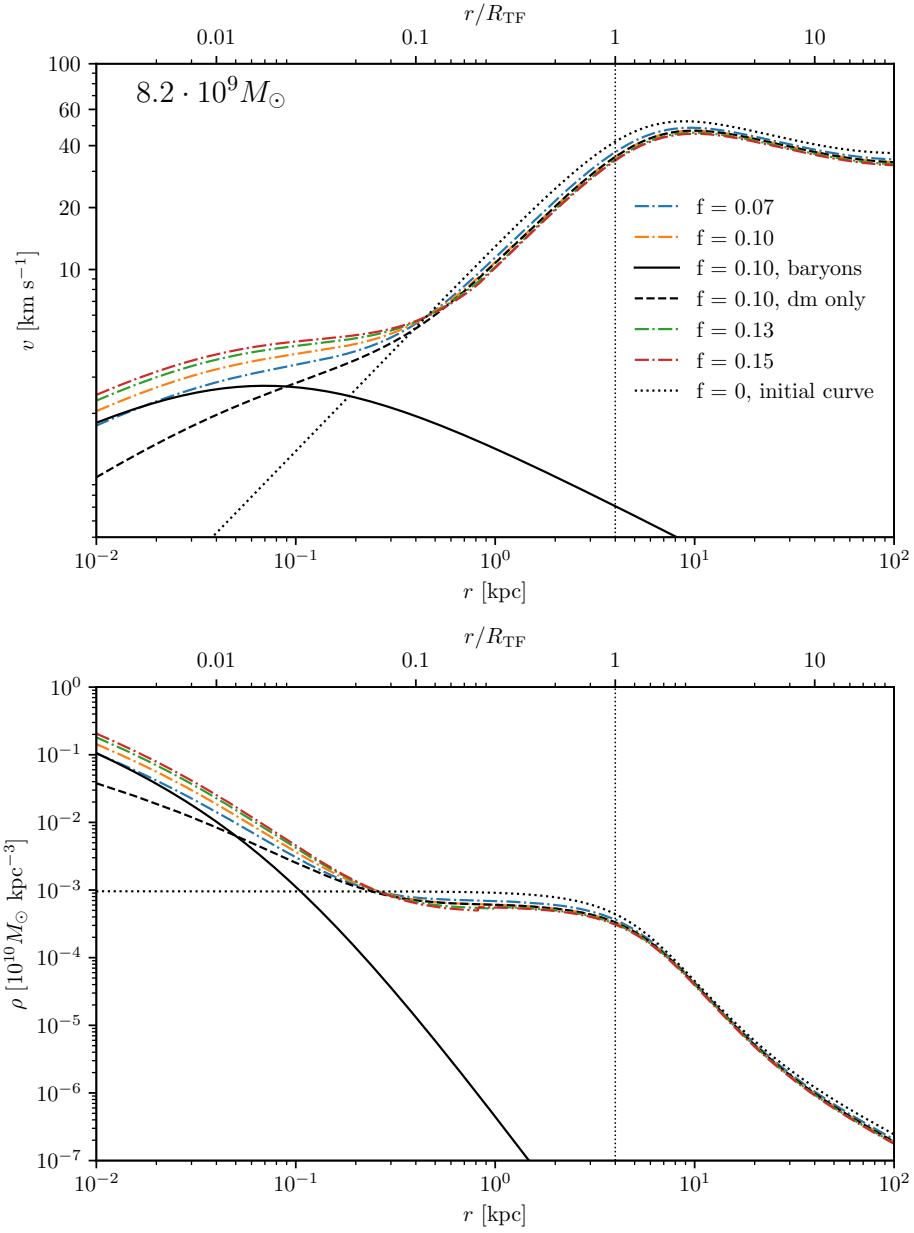

Figure 4.3: Adiabatically contracted SFDM halo in the Thomas-Fermi regime for a halo virial mass of $M = 8.2 \cdot 10^9 M_\odot$ and a core radius of $R_{\rm TF} = 4$ kpc. The vertical dotted line indicates this radius, where the transition from polytropic core to isothermal envelope occurs. *Top panel*: Velocity profiles. The outer part of the initial rotation curve (dotted line, $f = 0$) changes little during the contraction, while the baryons cause an increase of the velocity in the core regions. *Bottom panel*: Corresponding density profiles (same legend as above). Again, the density of the envelope remains almost unchanged and looks similar to the FDM case in Mocz et al. (2020) for this halo mass, while the core region experiences compression and thus a density increase of more than two orders of magnitude. This plot for the density profile may be compared with Figure 4 in Mocz et al. (2020).

the small-scale problems of cosmology. More precisely, they compared circular velocities of typical too-big-to-fail haloes with masses $M_{200} = 10^{9.5} - 10^{10} M_\odot$ for CDM and FDM to observational data for dwarf galaxies; i.e. isolated field galaxies and members of the Local Group that are, however, not satellites. Their results show an (expected) overprediction for the CDM case, while the FDM haloes fit the data well. Taking the same approach to further study typical cusp-core haloes with $M_{200} \sim 10^{11} M_\odot$, they compared circular velocities for CDM and FDM to those of galaxies from the SPARC database[4] for two different boson masses, $m_{22} = 0.8$ and $m_{22} = 2.5$, where m_{22} is defined as

$$m_{22} = \frac{m}{10^{-22}\ \mathrm{eV}}.$$

Their results reveal an exacerbation of the cusp-core problem for both FDM boson masses. This is because, when assuming isothermality, the mass-radius ratio of the soliton core should be approximately equal to that of the whole halo,

$$\frac{M_c}{\lambda_{\mathrm{deB}}} \approx \frac{M_{200}}{R_{200}} \propto M_{200}^{2/3},$$
$$M_c \sim M_{200}^{1/3},$$

resulting in the central density scaling as

$$\rho_0 \propto \frac{M_c}{\lambda_{\mathrm{deB}}^3} \propto M_c^4 \sim M_{200}^{4/3},$$

where M_c denotes the core mass of the halo, leading to the cored density profiles visible in Figure 2.6, which produce the correct slopes for haloes in that mass range. However, their amplitudes are too high to an extent that even CDM predictions are a better match to the observational data. Dawoodbhoy et al. (2021) performed a similar analysis focused on the Thomas-Fermi regime instead, again for halo masses in the range of $M_{200} = 10^{10} - 10^{11.15} M_\odot$. They showed that, when adjusting parameters in order to fit the smaller too-big-to-fail haloes, the circular velocity is overpredicted for small radii, both in CDM and FDM, when simulating high-mass dwarf galaxies. In contrast, the Thomas-Fermi regime with a core radius of $R_{\mathrm{TF}} = 4$ kpc matches the observational data for both halo mass ranges. However, the two studies were focused solely on the dark matter component and neglected possible baryonic effects in the core regions.

Our Figures 4.4 and 4.5 extend this work by also considering baryons and the gravitational effect they exert on the dark matter; the former shows our results using the Blumenthal method with constant $rM(r)$, whereas the latter shows our results applying the modification by Gnedin with constant $rM(\bar{r})$. From the density plots in the right panels of Figure 4.4 it is evident that

[4] http://astroweb.cwru.edu/SPARC/

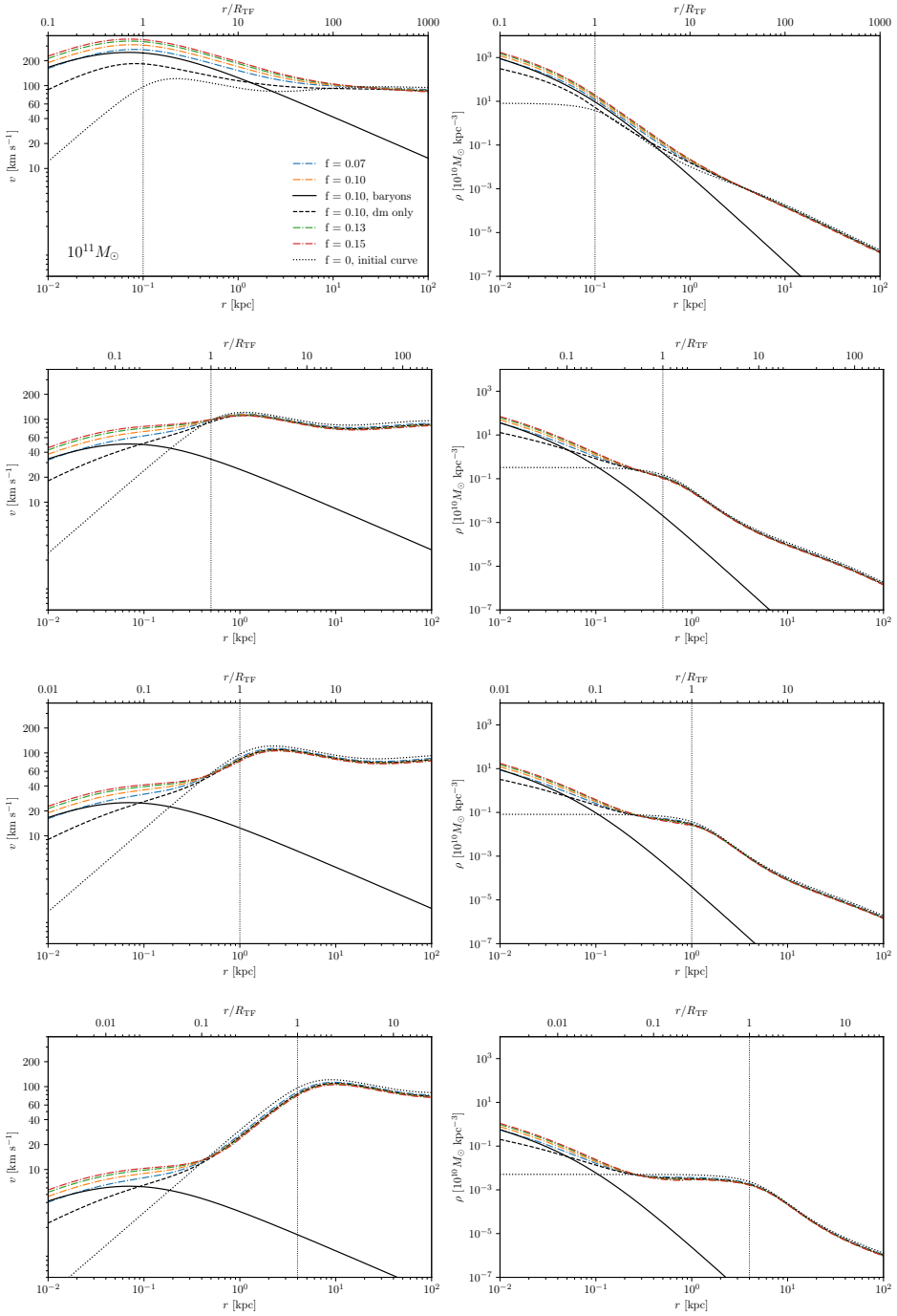

Figure 4.4: Adiabatic contraction with the Blumenthal method in the Thomas-Fermi regime for typical cusp-core haloes of $10^{11} M_\odot$. From top to bottom the chosen core radii are $R_{\rm TF} = 0.1, 0.5, 1, 4$ kpc. *Left panels*: Circular velocities for all four cases. One can see that small core radii lead to velocities $v_{\rm circ} > 200$ km s^{-1}, not compatible with observations of dwarf galaxies, while $R_{\rm TF} = 4$ kpc results in maximum velocities of $v_{\rm circ} \sim 100$ km s^{-1}. *Right panels*: Corresponding density profiles for all cases.

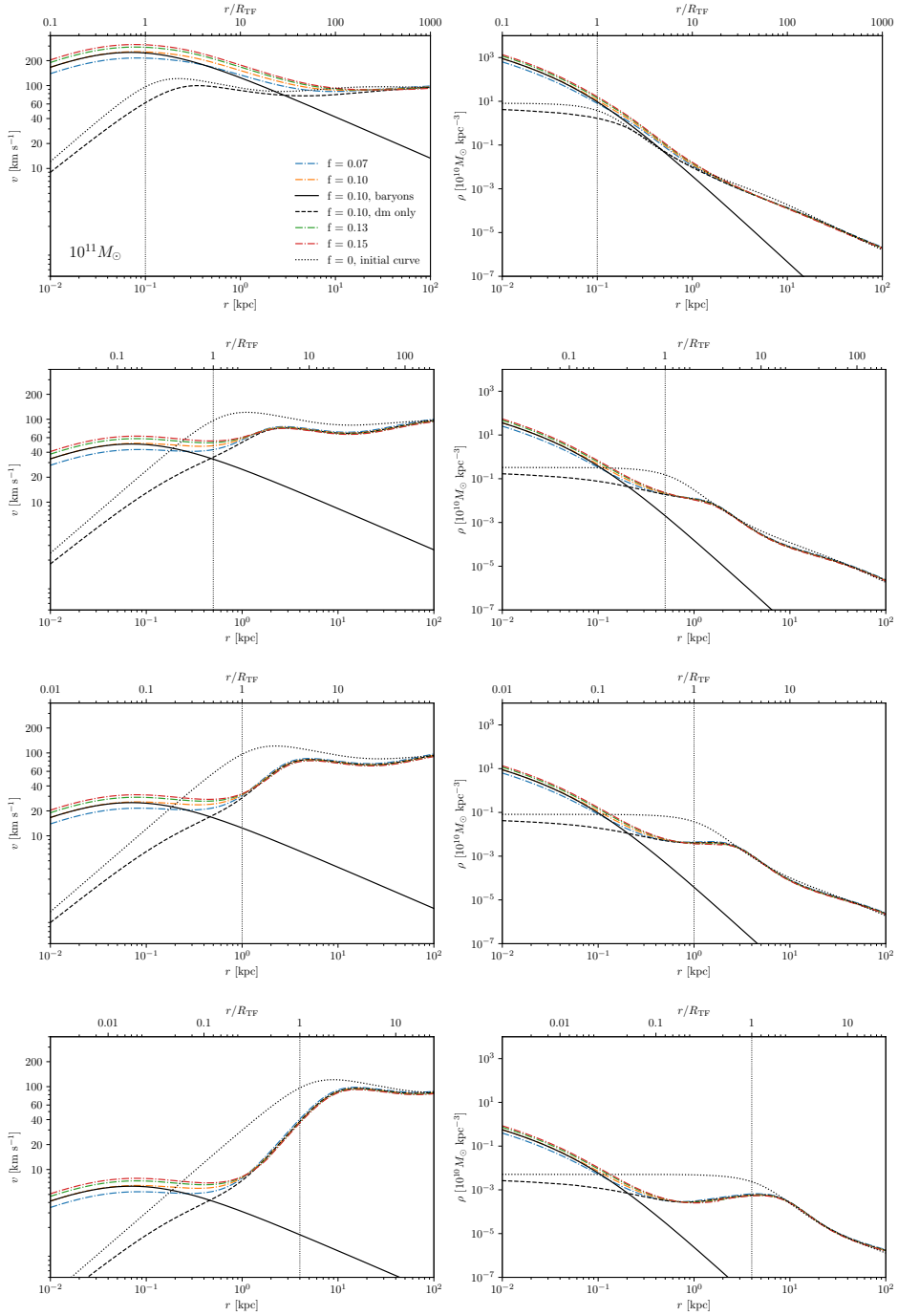

Figure 4.5: Adiabatic contraction with the modification by Gnedin in the Thomas-Fermi regime for the same cases as in Figure 4.4. *Left panels* again show circular velocities, *right panels* show their density profiles. The change of the adiabatic invariant to $rM(\bar{r})$ leads to a general density decrease of factor ≈ 2 in the innermost parts of the haloes, resulting in a corresponding decrease of circular velocities at these radii, compared to the Blumenthal method, as expected.

smaller core radii lead to much denser initial cores (e.g. the uppermost case with $R_{\mathrm{TF}} = 0.1$ kpc), which get compressed even further through adiabatic contraction. Assuming isothermality in the Thomas-Fermi regime, we have

$$\frac{M_c}{R_{\mathrm{TF}}} \approx \frac{M_{200}}{R_{200}} \propto M_{200}^{2/3},$$
$$M_c \sim M_{200}^{2/3}.$$

The central density therefore increases with decreasing R_{TF} as

$$\rho_0 \propto \frac{M_c}{R_{\mathrm{TF}}^3} \propto M_c \sim M_{200}^{2/3}, \tag{4.4}$$

while holding core and halo mass constant (Dawoodbhoy et al., 2021). This increase in density subsequently leads to an increase in circular velocity, as depicted in the left panels. The inclusion of baryons enhances the velocities to values higher than 200 km s^{-1} for the most extreme case, which is not observed in dwarf galaxies in the Universe. On the other hand, larger core radii of 4 kpc show velocity curves consistent with observations and aforementioned publications; despite the contraction in the innermost ~ 200 pc, the velocity at these radii does not exceed values of 15 km s^{-1}. The applied modification by Gnedin shown in Figure 4.5 confirms this picture with similar results. However, the adjustment for eccentric orbits leads to a general decrease in density around the core radius by a factor of ≈ 2, which is in agreement with Gnedin et al. (2004). This, in turn, causes the velocity to drop more sharply, which then again flattens out for the innermost regions. Like for the Blumenthal method, larger core radii can reproduce observed rotation curves of dwarf galaxies, while small cores lead to velocities exceeding even that of the Milky Way.

For the sake of comparison, Figure 4.6 shows our results for adiabatic contraction of a CDM halo with an NFW profile,

$$\rho_{\mathrm{NFW}}(r) = \frac{\delta_{\mathrm{NFW}} \rho_{\mathrm{crit}}}{(cr/R_{200})\,(1 + cr/R_{200})^2}, \tag{4.5}$$

where $c = 10$ is the halo concentration parameter, suitable for a halo mass of $M = 10^{11} M_\odot$ according to the mass-concentration relation by Klypin et al. (2016), $\rho_{\mathrm{crit}} = 3H_0^2/8\pi G$ is the current critical background density and with

$$\delta_{\mathrm{NFW}} = \frac{\Delta_{\mathrm{crit}}}{3} \frac{c^3}{\ln(1+c) - c/(1+c)}. \tag{4.6}$$

$\Delta_{\mathrm{crit}} = 200$ describes the mean overdensity of a halo compared to ρ_{crit}, and the Hubble parameter is chosen as $H_0 = 70$ km s^{-1} Mpc^{-1}. The initial rotation curve reaches its maximum of $v_{\mathrm{circ}} \sim 90$ km s^{-1} at a radius of $r \sim 23$ kpc. Because the NFW profile is a cuspy profile rather than the cored one of the Thomas-Fermi regime, the central regions of the halo are naturally denser even in the absence of baryons, leading to higher initial rotational velocites at these

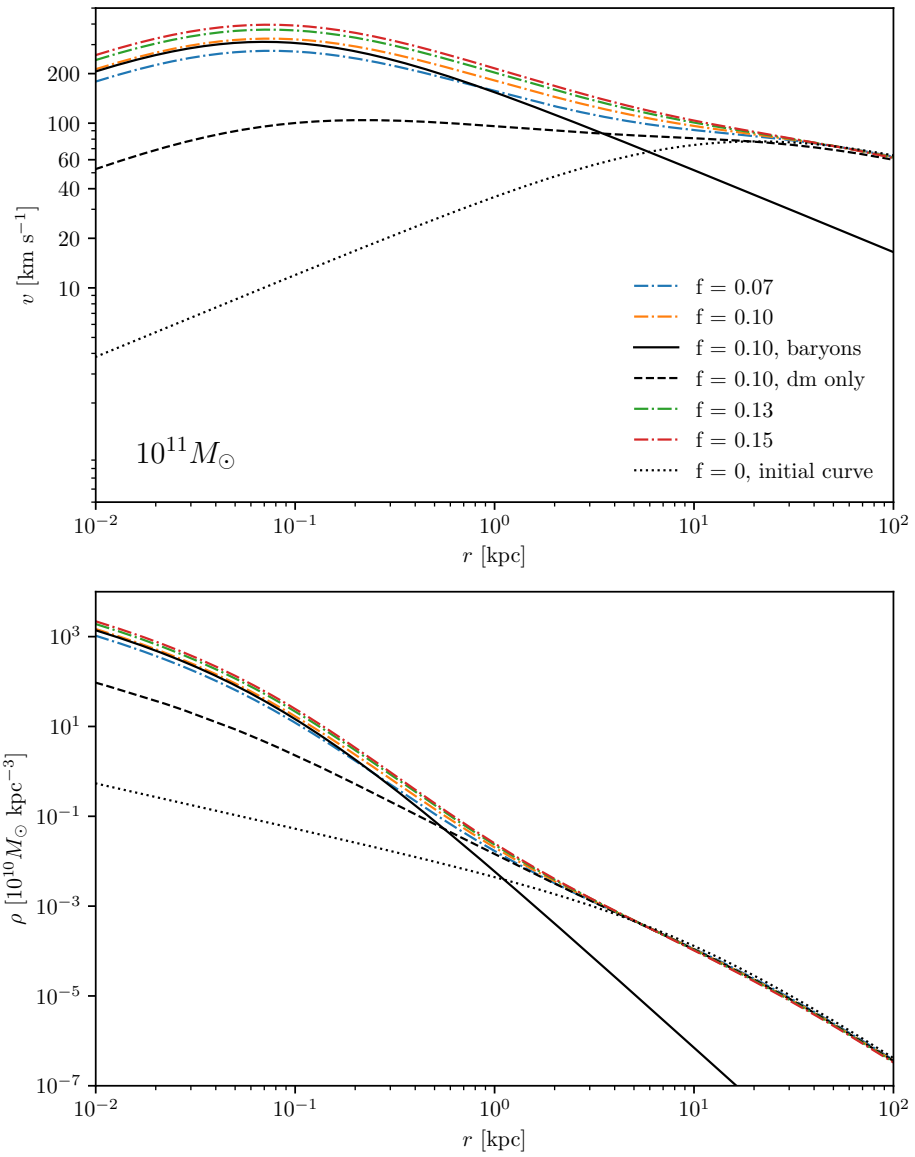

Figure 4.6: Adiabatic contraction with the Blumenthal method for a CDM halo with an initial NFW profile (dotted line), $M_{200} = 10^{11} M_\odot$ and concentration parameter $c = 10$. *Top* panel shows circular velocities, *bottom* panel shows the corresponding density profiles. The cuspy nature of the initial dark matter profile leads in general to an overprediction of circular velocities in the inner regions even without baryons. The inclusion of the latter worsens this effect substantially, resulting in velocities that exceed 200 km s^{-1}, comparable to the Thomas-Fermi regime with $R_{\rm TF} = 0.1$ kpc (shown in the uppermost panels of Figures 4.4 and 4.5).

radii. The gravitational effect of the baryons enhances the density by at least three orders of magnitude for radii $r \lesssim 0.1$ kpc. The resulting circular velocity curve is similar to that obtained for the Thomas-Fermi regime with core radius $R_{\mathrm{TF}} = 0.1$ kpc, with velocities exceeding the observed values at these radii by at least 100 km s^{-1}, leading to an aggravation of the cusp-core problem.

Our findings now suggest that adiabatic contraction due to baryons requires kpc-sized SFDM cores in order to be in accordance with observations of rotation curves of dwarf galaxies. Furthermore, when baryons are included, small SFDM cores in the Thomas-Fermi regime lead to central velocity profiles which are in conflict with observations, for the velocities are comparable to those obtained for initial NFW profiles in the CDM case, reaching values higher than 200 km s^{-1} for both cases. The same issue may arise for FDM haloes, if their cores are too small; this issue may be resolved in the future, when simulations are able to resolve sub-kpc cores, which is not possible nowadays. Now, recent work by Shapiro et al. (2021) strongly suggests that kpc-sized cores in the Thomas-Fermi regime are disfavoured on the grounds that structure formation of the corresponding haloes is suppressed, while haloes with small cores are not. In conjunction with our results here, it therefore appears that the parameter range of viable SFDM core sizes is severely restricted, implying potentially severe constraints for the SFDM model. It remains to be seen whether more accurate calculations and simulations in the future will confirm our conclusions, and what that entails for SFDM as a candidate for dark matter.

Chapter 5

Summary and conclusions

In this work, we have considered a promising alternative to standard cold dark matter, that is scalar field dark matter (SFDM). In this theory, dark matter consists of ultra-light bosons with masses of $m \sim 10^{-22}$ eV that form gravitationally bound haloes. SFDM can suppress formation of structure on subgalactic scales, while behaving like standard CDM on larger scales and thus serving as probable solution to the small-scale problems of cosmology. Two regimes are presented; the fuzzy regime, where a quantum potential acts against gravity, and the Thomas-Fermi regime with strong repulsive self-interaction. The focus of this thesis lies in the latter and therefore provides a thorough calculation of analytical expressions for density, gravitational potential and circular velocity in a static and spherically symmetric configuration. This configuration represents the core regions of dark matter haloes comprised of Bose-Einstein condensed bosons, with its characteristic core radius R_{TF}, given in equation (2.16), which is only dependent on the strength of self-interaction g, and the particle mass m. For a complete physical picture and further analysis, this core region is then embedded in an isothermal, CDM-like envelope.

Based upon the Gross-Pitaevskii equation (2.1), the fundamental equation of this theory, it is possible to construct the Hamiltonian of such a system, which further enables the calculation of action-angle variables, a set of generalized coordinates and conjugate momenta useful for particles in rotational motion. The actions, which represent the momenta, and their angles, the generalized coordinates, define an invariant torus on which the particles move. This new set of coordinates provides a twofold advantage; firstly they allow to calculate orbits, and secondly the actions remain constant for variations in the gravitational potential, as long as these variations are slow compared to typical orbital frequencies - a characteristic that can be heavily exploited for more detailed analysis. The former is achieved through the derivation of a Quantum-Hamilton-Jacobi equation and subsequently solving it through separation of variables of the action function S. It is shown that this separation ansatz is feasible through verification that the so-called Stäckel conditions are fulfilled; ensuing calculations then provide the solutions of the radial, polar

and azimuthal actions, $J_r, J_\vartheta, J_\varphi$ respectively. Numerical orbit calculation is achieved using the Python package `gala`, which reveals almost circular orbits for arbitrarily chosen, physically motivated initial conditions in the core regions of haloes in the Thomas-Fermi regime with given radius R_{TF}.

The second characteristic of the action-angle variables, the actions' constancy in slowly changing gravitational potentials, opens up the study of the so-called adiabatic contraction. Developed by Blumenthal et al. (1986), it calculates the response of dark matter particles to the presence of a baryonic accumulation located in the center of a halo. It is based upon the assumption of circular orbits within a spherically symmetric mass distribution $M(r)$, an assumption verified in the first part of the thesis to be appropriate in the context of the Thomas-Fermi regime in SFDM cosmologies. The adiabatic invariant $rM(r)$ of a particle orbit in such a system then suggests that

$$r_f \left[M_{\mathrm{dm}}(r_f) + M_b(r_f)\right] = r_i M_i(r_i) = r_i \frac{M_{\mathrm{dm}}(r_f)}{1-f},$$

with initial radius r_i, final radius r_f, initial (total) mass distribution $M_i(r_i)$ and final mass distributions $M_{\mathrm{dm}}(r_f)$ and $M_b(r_f)$, for the dark matter and baryon components, respectively. This equation is solved iteratively with Python and enables to calculate circular velocity and density profiles for a given halo configuration. However, it is shown in the literature that dark matter particle orbits are not limited to the circular case and highly eccentric orbits are also possible. This fact is accounted for by the modification of Gnedin et al. (2004), which changes the adiabatic invariant to $rM(\bar{r})$, where $\bar{r}$ represents an orbit-averaged radius. With these two models it is possible to compare our results to available literature on the topic, both for the fuzzy and self-interacting regime. These previous studies are almost entirely focused on the dark matter component and did mostly not factor in the gravitational effects of baryons. Nevertheless, they provide evidence that SFDM as a whole is a viable option in solving the small-scale problems.

Mocz et al. (2020) show the evolution of a fuzzy dark matter (FDM) Universe down to a redshift of $z = 5.5$, in which they idenfity three dark matter haloes with different size and mass; they show their density profiles at $z = 6$. We simulated the largest of these haloes, halo 1 with $M_{200} = 8.2 \cdot 10^9 M_\odot$, using our adiabatic contraction code. In order to obtain comparable core densities to the FDM case, the Thomas-Fermi regime requires core sizes substantially larger than FDM, by even a factor of 4. The inclusion of baryons, however, barely alters the density profile outside the cores. Only in the inner regions this gravitational effect is significant and increases the density by at least two orders of magnitude, implying enhanced circular velocities, though only by less than 10 km s^{-1}.

In the context of the small-scale problems, Robles et al. (2019) show that FDM can describe rotational velocities of typical too-big-to-fail haloes ($M_{200} \sim 10^{10} M_\odot$) better than standard CDM. However, applying the same method to

typical cusp-core haloes with $M_{200} \sim 10^{11} M_\odot$ results in an overprediction for the FDM case (as well as for CDM, as expected). Dawoodbhoy et al. (2021) extend this work to the Thomas-Fermi regime by tuning parameters such that the velocities provide a good match for this mass range, and subsequently also analyze high-mass dwarf haloes, representative for the cusp-core problem. They confirm the overprediction for CDM and FDM when shifting to these higher masses, and show that the Thomas-Fermi regime produces good fits to observational data on rotational velocities for dwarf galaxies of this mass for a core radius of $R_{\mathrm{TF}} = 4$ kpc.

This thesis studies the addition of baryons and the effect they pose on the dark matter particles with respect to the question of gravitational contraction. Using the Blumenthal method, as well as the Gnedin modification, the findings can be summarized as follows:

1. Adiabatic contraction due to baryons suggests core radii $R_{\mathrm{TF}} \gtrsim 1$ kpc in order to produce rotational velocities comparable to observations of dwarf galaxies. Smaller cores lead to higher initial density, which get further increased through compression caused by the baryons; the resulting velocities exceed even that of massive spiral galaxies like the Milky Way. This issue may also arise for FDM with too small solitonic cores. However, in order to verify this result with cosmological simulations, higher resolution in these simulations will be required in the future.

2. In the CDM case for a typical cusp-core halo ($M_{200} \sim 10^{11} M_\odot$), adiabatic contraction worsens the cusp-core problem by increasing the already high density at small radii even further, reaching values of $\rho \sim 10^{13} M_\odot$ kpc^{-3} at $r \lesssim 100$ pc. The resulting rotational velocities are comparable to the SFDM case in the Thomas-Fermi regime with sub-kpc core radii, $R_{\mathrm{TF}} = 0.1$ kpc, not compatible with observations.

3. The baryon fraction, individual for each halo, has only small effects on the outer final density and velocity profiles. Outside the core these profiles resemble the initial curve, with most changes occuring inside the core. However, the resulting density profiles with realistic baryon fractions of $f = 0.07 - 0.15$ almost lie on top of each other, causing velocity changes of only a few km s^{-1} between the considered cases.

4. A comparison of the Blumenthal method with the modification by Gnedin (Figures 4.4 and 4.5) for several core radii reveals the (expected) decrease of the density by a factor of roughly 2 at a distance of around R_{TF} from the center for the latter, thus being in accordance with Gnedin et al. (2004). Despite this quite substantial decrease in density, the velocity at these radii only changes slightly and provides qualitatively the same results as the Blumenthal method.

5. In contrast to the suggested kpc-sized Thomas-Fermi cores in item 1., recent studies favour sub-kpc cores on the basis of structure formation.

This dichotomy leads to a severe restriction of the parameter range for viable SFDM core sizes, further implying potentially strong constraints on the SFDM model.

Appendix A

Action-angles for the isochrone potential

So far we have seen orbits and their corresponding actions for dark matter particles in a $(n = 1)$-polytrope potential, eq. (2.19). As these actions were integrals of motion, it was necessary to solve them numerically through orbit integration and coordinate transformation. This section is now dedicated to carry out the calculations for the isochrone potential (Henon (1959a), Henon (1959b)),

$$\Phi(r) = -\frac{GM}{b + \sqrt{b^2 + r^2}}, \tag{A.1}$$

one of the few potentials for which the whole procedure is possible analytically. Here, b represents a (constant) scale factor, which defines the region where the potential is similar to that of a homogeneous sphere. As mentioned previously, one limiting case of the isochrone potential is the Kepler potential. This can be seen when $b \to 0$, or equivalently, when $r \gg b$. Equation (A.1) then reduces to

$$\Phi(r) = -\frac{GM}{r}.$$

On the other hand, when $r/b \to 0$, or $b \gg r$, equation (A.1) can be expanded around r/b and reads

$$\Phi(r) = -\frac{GM}{b\left(1 + \sqrt{(r/b)^2 + 1}\right)} \approx -\frac{GM}{b\left(2 + \frac{1}{2}(r/b)^2\right)} = \frac{GM}{8b^3} r^2 + \text{const.},$$

which represents the potential of a homogeneous sphere.

For the sake of completeness, let us start with the construction of the Lagrangian. The most basic assumption is a single particle moving in a circular orbit. Throughout this thesis spherical symmetry was assumed, thus a switch to the more convenient spherical coordinate system makes sense, and this is

accomplished through

$$\begin{aligned} x &= r \sin\vartheta \cos\varphi, \\ y &= r \sin\vartheta \sin\varphi, \\ z &= r \cos\vartheta. \end{aligned}$$

The Lagrangian is defined as

$$\mathcal{L} = T - U,$$

where T represents the kinetic energy and U stands for the potential energy, which is connected to the gravitational potential Φ through

$$\Phi = \frac{U}{m}. \tag{A.2}$$

For a single-particle system,

$$T = \frac{mv^2}{2},$$

thus the velocity of the particle is required. Taking the derivatives of the positions (with respect to time),

$$\begin{aligned} \dot{x} &= \dot{r} \sin\vartheta \cos\varphi + r\dot{\vartheta} \cos\vartheta \cos\varphi - r\dot{\varphi} \sin\vartheta \sin\varphi, \\ \dot{y} &= \dot{r} \sin\vartheta \sin\varphi + r\dot{\vartheta} \cos\vartheta \sin\varphi + r\dot{\varphi} \sin\vartheta \cos\varphi, \\ \dot{z} &= \dot{r} \cos\vartheta - r\dot{\varphi} \sin\varphi, \end{aligned}$$

the velocity can be calculated in terms of the new coordinates. After some algebra this results in

$$v^2 = \dot{x}^2 + \dot{y}^2 + \dot{z}^2 = \dot{r}^2 + r^2\dot{\vartheta}^2 + r^2\dot{\varphi} \sin^2\vartheta^2,$$

and the Lagrangian reads

$$\mathcal{L} = \frac{m}{2}\left(\dot{r}^2 + r^2\dot{\vartheta}^2 + r^2\dot{\varphi}^2 \sin^2\vartheta\right) - U.$$

Next, the definition of the Hamiltonian of a system,

$$\mathcal{H} = \left(\sum_i p_i \dot{q}_i\right) - \mathcal{L},$$

is used, with the generalized coordinates q_i and the corresponding generalized momenta p_i. These are defined as

$$p_i = \frac{\partial \mathcal{L}}{\partial \dot{q}_i},$$

thus the three generalized momenta for the system are

$$p_r = \frac{\partial \mathcal{L}}{\partial \dot{r}} = m\dot{r}, \qquad p_\vartheta = \frac{\partial \mathcal{L}}{\partial \dot{\vartheta}} = mr^2\dot{\vartheta} \qquad \text{and} \qquad p_\varphi = \frac{\partial \mathcal{L}}{\partial \dot{\varphi}} = mr^2\dot{\varphi}\sin^2\vartheta.$$

Inserting these expressions into the Hamiltonian yields

$$\begin{aligned}\mathcal{H} &= p_r\dot{r} + p_\vartheta\dot{\vartheta} + p_\varphi\dot{\varphi} - \left(\frac{m}{2}\left[\dot{r}^2 + r^2\dot{\vartheta}^2 + r^2\dot{\varphi}^2\sin^2\vartheta\right] - m\Phi\right) \\ &= \frac{1}{2m}\left(p_r^2 + \frac{p_\vartheta^2}{r^2} + \frac{p_\varphi^2}{r^2\sin^2\vartheta}\right) + m\Phi,\end{aligned}$$

where additionally equation (A.2) is used. Comparing this expression to the Hamiltonian in equation (3.3), one can see that the only difference is the potential; here solely the gravitational potential is relevant. From this it is evident that separation of variables is feasible, and, through the same calculations as in Section 3, the actions yield

$$J_\varphi = \frac{1}{2\pi}\int \mathrm{d}\varphi L_z, \tag{A.3}$$

$$J_\vartheta = \frac{1}{2\pi}\int \mathrm{d}\vartheta\sqrt{L^2 - \frac{L_z^2}{\sin^2\vartheta}}, \tag{A.4}$$

$$J_r = \frac{1}{2\pi}\int \mathrm{d}r\sqrt{2m\left(E-\Phi\right) - \frac{L^2}{r^2}}. \tag{A.5}$$

To solve these three integrals it is necessary to figure out their limits, thus one needs to know the relevant curve of each coordinate (Binney and Tremaine, 2008). Since a particle on a circular orbit is assumed, φ changes in the interval $[0, 2\pi]$ and therefore the azimuthal action, eq. (A.3), results in

$$J_\varphi = \frac{1}{2\pi}\int_0^{2\pi} \mathrm{d}\varphi L_z = L_z.$$

Carrying on with the change of the polar angle, there is always a smallest value that ϑ occupies during the orbit, $\vartheta_{\min} \leq \pi/2$, given by

$$\sin\vartheta_{\min} = \frac{|L_z|}{L}.$$

The integrand reaches its maximum at this position and equals zero for $\pi - \vartheta_{\min}$. Since this equals an integration over only a quarter period of the integrand, multiplication by 4 is needed. Thus the latitudinal action results in

$$J_\vartheta = \frac{2}{\pi}\int_{\pi/2}^{\pi-\vartheta_{\min}} \mathrm{d}\vartheta\sqrt{L^2 - \frac{L_z^2}{\sin^2\vartheta}} = L - |L_z|.$$

Lastly, the radial action is quite a bit more complicated to calculate, since here the gravitational potential comes into play. Because the isochrone potential

is chosen, one can make use of a fundamental property of it, namely that the radial frequency being only dependent on its energy[1], so that

$$\frac{\partial \mathcal{H}}{\partial J_r} = \frac{\partial E}{\partial J_r} = \omega_r(E). \tag{A.6}$$

When the radial action, eq. (A.5), gets written in terms of the generalized momentum p_r, the equation can be rearranged to get an expression for the radial period T_r,

$$T_r = 2\int_{r_{\mathrm{peri}}}^{r_{\mathrm{apo}}} \frac{\mathrm{d}r}{\sqrt{2m(E-\Phi) - L^2/r^2}}, \tag{A.7}$$

with the radii of apocenter and pericenter, respectively. To solve this integral, an auxiliary variable is defined,

$$s = -\frac{GM}{b\Phi} = \frac{b+\sqrt{b^2+r^2}}{b} = 1+\sqrt{1+\frac{r^2}{b^2}} \qquad \Longleftrightarrow \qquad r^2 = b^2s^2 - 2b^2s,$$

and therefore

$$r\mathrm{d}r = b^2(s-1)\mathrm{d}s.$$

With these expressions, equation (A.7) becomes

$$\begin{aligned} T_r &= 2\int_{r_{\mathrm{peri}}}^{r_{\mathrm{apo}}} \frac{r\mathrm{d}r}{\sqrt{2mr^2(E-\Phi) - L^2}} = 2\int_{s_1}^{s_2} \frac{b^2(s-1)\mathrm{d}s}{\sqrt{2m(b^2s^2-2b^2s)(E-\Phi) - L^2}} \\ &= 2\int_{s_1}^{s_2} \frac{b(s-1)\mathrm{d}s}{\sqrt{2mEs^2 - 2ms(2E+s\Phi) + 4ms\Phi - L^2/b^2}} \\ &= 2\int_{s_1}^{s_2} \frac{b(s-1)\mathrm{d}s}{\sqrt{2mEs^2 - 2ms(2E-GM/b) - 4GMm/b - L^2/b^2}}, \end{aligned}$$

with s_1 and s_2 as new limits, within which the argument of the square root is positive. They are defined as

$$s_1 + s_2 = 2 - \frac{GM}{Eb} \qquad \text{and} \qquad s_1 s_2 = -\frac{L^2 + 4GMmb}{2Eb^2}.$$

These can be used to finally solve the integral,

$$\begin{aligned} T_r &= 2\int_{s_1}^{s_2} \frac{b(s-1)\mathrm{d}s}{2mE(s^2 - s(s_1+s_2) + s_1s_2)} = \frac{2b}{\sqrt{-2mE}}\int_{s_1}^{s_2} \frac{(s-1)\mathrm{d}s}{(s_2-s)(s-s_1)} \\ &= \frac{2b}{\sqrt{-2mE}}\left(\frac{s_1+s_2}{2} - 1\right) = \frac{2\pi GM}{\sqrt[3]{-2mE}}. \end{aligned}$$

[1] However, there are alternative ways to solve this problem, e.g. making use of the integration of complex analytic functions and the theorem of residues.

With this expression, equation (A.6) for the radial frequency can now be integrated,

$$J_r = \int \frac{\mathrm{d}E}{\omega_r(E)} + f(L) = \frac{GM}{\sqrt{-2mE}} + f(L), \tag{A.8}$$

with $f(L)$ being an unknown function depending only on the angular momentum that still needs to be determined. To specify this function, one can make use of the property of circular orbits, for which the action integral is zero, i.e.

$$v_r = p_r = 0 \qquad \Rightarrow \qquad J_r = 0.$$

Furthermore, there exists an equilibrium between gravitational and centrifugal force (Boccaletti and Pucacco, 2004), represented by

$$v_c^2 = v_\vartheta^2 + v_\varphi^2 = r\frac{\mathrm{d}\Phi}{\mathrm{d}r} = r\frac{\mathrm{d}}{\mathrm{d}r}\left(-\frac{GM}{b+\sqrt{b^2+r^2}}\right) = \frac{GMr^2}{\sqrt{b^2+r^2}\left(b+\sqrt{b^2+r^2}\right)^2}.$$

The energy of a circular orbit, E_c, is then simply

$$\begin{aligned} E_c = \frac{1}{2}mv_c^2 + m\Phi &= \frac{1}{2}\frac{GMm(a^2-b^2)}{a\,(a+b)^2} - \frac{GMm}{a+b} \\ &= \frac{GMm(a-b) - 2aGMm}{2a(a+b)} = -\frac{GMm}{2a}, \end{aligned}$$

with $a = \sqrt{b^2+r^2}$, whereas its corresponding angular momentum results in

$$\begin{aligned} L_c = rv_c = \frac{\sqrt{GM}(a^2-b^2)}{\sqrt{a}(a+b)} &= \frac{\sqrt{GM}(a-b)}{\sqrt{a}} = \frac{\sqrt{a}GM}{\sqrt{GM}} - \frac{b\sqrt{GM}}{\sqrt{a}} \\ = \frac{GM}{\sqrt{-2E_c}} - b\sqrt{-2E_c} &= \sqrt{GMb}\left(\sqrt{-\frac{GM}{2E_cb}} - \sqrt{-\frac{2E_cb}{GM}}\right). \end{aligned} \tag{A.9}$$

The goal is that J_r in equation (A.8) vanishes, thus $f(L)$ must satisfy

$$f(L) = f(L_c) = -\frac{GM}{\sqrt{-2E_c}} = -\sqrt{\frac{GMb}{\lambda}},$$

where another auxiliary variable,

$$\lambda = -\frac{2E_cb}{GM}, \qquad 0 \le \lambda \le 1,$$

is used. From the angular momentum for circular orbits, eq. (A.9), one can see that

$$\frac{L_c}{\sqrt{GMb}} = \left(\lambda^{-1/2} - \lambda^{1/2}\right) = \frac{1-\lambda}{\sqrt{\lambda}}.$$

Solving the quadratic equation for $\sqrt{\lambda}$ yields

$$\sqrt{\lambda} = \frac{-L \pm \sqrt{L^2 + 4GMb}}{2\sqrt{GMb}},$$

where only the solution with plus sign is physically relevant. Thus, the unknown function $f(L)$ is determined to be

$$f(L) = -\sqrt{\frac{GMb}{\lambda}} = \frac{2GMb}{L - \sqrt{L^2 + 4GMb}} = -\frac{1}{2}\left(L + \sqrt{L^2 + 4GMb}\right),$$

and the desired analytical solution for the radial action of the system finally reads

$$J_r = \frac{GM}{\sqrt{-2mE}} - \frac{1}{2}\left(L + \sqrt{L^2 + 4GMb}\right). \tag{A.10}$$

Appendix B

Adiabatic contraction Python code

Although the code is relatively short, this Appendix gives a step-by-step explanation on subsequent excerpts of it. Starting with the import of necessary Python modules, it is then necessary to define several functions; the first one serves for solving the differential equation (2.26), the second and third define a variety of dark matter and baryon mass profiles analytically.

```
import numpy as np
import matplotlib.pyplot as plt
from scipy.integrate import solve_ivp

#plt.rcParams.update({
#    "text.usetex": True,
#    "font.family": "DeJavu Serif",
#    "font.sans-serif": ["Helvetica"]})
#plt.rcParams['lines.linewidth'] = 1

def dpsi_dxi(xi, psi): # ODE from Chavanis (2019) / Method 1
    return [psi[1], (chi * psi[1]**2 + 1)/(chi + np.exp(psi[0])) - 2 * psi[1]
    / xi]

def M_dm(r, R, DM_PROFILE):
    if DM_PROFILE == 'polytrope':       # n=1 polytrope
        return 4 * rho_dm * R**3 / np.pi**2 * (np.sin(np.pi * r / R) - np.pi *
     r / R * np.cos(np.pi * r / R))
    elif DM_PROFILE == 'pis':           # pseudo-isothermal sphere
        return 4 * rho_dm * np.pi * R**2 / 9 * (3 * r - np.sqrt(3) * R * np.
    arctan(np.sqrt(3) * r / R))
    elif DM_PROFILE == 'nfw':           # nfw
        return 4 * rho_dm * np.pi * R**3 * (np.log((R + r) / R) + R / (R + r)
    - 1)
    elif DM_PROFILE == 'nfwc':          # nfw with concentration parameter
        return 4 * rho_dm * np.pi * R**3 * (np.log(1 + c * r) - c * r / (1 + c
     * r))
    elif DM_PROFILE == 'burkert':       # burkert profile
        return rho_dm * np.pi * R**3 * (2 * np.log(1 + r / R) + np.log(1 + r
    **2 / R**2) - 2 * np.arctan(r / R))

def M_b(r, b, BARYON_PROFILE):
    if BARYON_PROFILE == 'exp':         # exp. surface brightness profile
        return (1 - (1 + r/b) * np.exp(- r/b)) * 2 * np.pi * b**2 * rho_b
    elif BARYON_PROFILE == 'hernquist': # hernquist profile
        return r**2 * (1 + b)**2 / (r + b)**2 * 2 * np.pi * b * rho_b
    elif BARYON_PROFILE == 'jaffe':     # jaffe profile
        return r / (r + b)
```

```
    elif BARYON_PROFILE == 'burkert':   # burkert profile
        return rho_b *np.pi * b**3 * (2 * np.log(1 + r / b) + np.log(1 + r**2
    / b**2) - 2 * np.arctan(r / b))
```

The next step is to choose which profiles should be examined as well as their associated parameters, such as the baryonic scale length `b` or the halo mass `M200`. Furthermore, it is necessary to define an initial radius `ri` on which the contraction shall be calculated.

```
# available dm profiles: 'polytrope', 'pis', 'nfw', 'nfwc', 'burkert', '
    envelope'
DM_PROFILE = 'envelope'
# available baryon profiles: 'exp', 'hernquist', 'jaffe', 'burkert'
BARYON_PROFILE = 'hernquist'

b = 0.07    # scale factor for baryonic profile
c = 2       # concentration parameter for nfw profile
chi = 1

M200 = 1e11    # total halo mass in Msol
R200 = 96      # virial radius in kpc

R_TF = 4                          # core radius in kpc
f = [0.07, 0.1, 0.13, 0.15]       # baryon fractions
pc = 3.0857e16                    # kpc in m for result conversion
G = 4.516e-30                     # gravitational constant in pc^3 / Msol / s^2

rho_dm = np.pi / 4 * M200 * chi / (R200 * R_TF**2) / 1e9

#rho_dm = 0.2        # fixed central density of dwarf galaxy from burkert2015
                     # in Msol / pc^3
rho_b = rho_dm       # baryon density

fig, axs = plt.subplots(2, 1, figsize = (6, 9), squeeze=False)
ri = np.logspace(-4, 6, 3000)
Minit = np.empty(len(ri))
```

Having everything defined, the following part ensures that, depending on the initial dark matter profile chosen, the enclosed mass at each radius gets stored into an array. When the keyword `envelope` is chosen, the program first solves the differential equation for the Thomas-Fermi regime plus envelope using a DOP853 solver (i.e. an explicit Runge-Kutta method of 8th order), otherwise this step is not necessary.

```
if DM_PROFILE == 'envelope':
    psis = solve_ivp(dpsi_dxi, [ri[0], ri[-1]], [0, 0], method='DOP853',
    t_eval=ri)

    ys = rho_dm * np.exp(-psis.y[0])
    ri = np.logspace(-4, 6, 3000) * R_TF / np.sqrt(chi) / np.pi

    Minit[0] = 4 * np.pi / 3 * ri[0]**3
    for i in range(1, len(ri)):
        Minit[i] =  Minit[i-1] + 4 * np.pi / 3 * (ri[i]**3 - ri[i-1]**3) * ys[
    i]
else:
    for i in range(len(Minit)):
        Minit[i] = M_dm(ri[i], R_TF, DM_PROFILE)
```

The ensuing part is the code's centerpiece as it iterates through the initial radius and compares the constant expression $r_i M(r_i)$ to the final mass profile,

combined from dark matter and baryons, times the radius. In order to assure a smooth curve, the steps of this iteration process become smaller and smaller.

```
for j in range(len(f)):
    Mdm = np.empty(len(ri))
    Mdm = (1 - f[j]) * Minit
    rf = np.zeros(len(ri))
    for i in range(len(ri)):
        r = ri[i]
        while (r * (Mdm[i] + f[j] * M_b(r, b, BARYON_PROFILE))) >= (ri[i] *
    Minit[i]):
            r = r*.9
        r = r/.9
        while (r * (Mdm[i] + f[j] * M_b(r, b, BARYON_PROFILE))) >= (ri[i] *
    Minit[i]):
            r = r*.99
        r = r/.99
        while (r * (Mdm[i] + f[j] * M_b(r, b, BARYON_PROFILE))) >= (ri[i] *
    Minit[i]):
            r = r*.999
        r = r/.999
        while (r * (Mdm[i] + f[j] * M_b(r, b, BARYON_PROFILE))) >= (ri[i] *
    Minit[i]):
            r = r*.9999
        r = r/.9999
        while (r * (Mdm[i] + f[j] * M_b(r, b, BARYON_PROFILE))) >= (ri[i] *
    Minit[i]):
            r = r*.99999
        rf[i] = r/.999999
```

The last important part of the code is to choose whether the Blumenthal method or the modification by Gnedin shall be used in order to compute the final mass profile. From this profile the rotational velocities and densities are calculated numerically. The rest of the code is then simply the plotting routine.

```
    #rf = R200 * 0.85 * (rf / R200)**0.8        # for Gnedin04 version
    Mbar = np.zeros(len(rf))
    for i in range(len(rf)):
        Mbar[i] = M_b(rf[i], b, BARYON_PROFILE) * f[j]

    Mfin = Mdm + Mbar

    densdm, densb, densfin = np.zeros(len(rf)), np.zeros(len(rf)), np.zeros(
    len(rf))
    densdm[0] = 3 * Mdm[0] / (4 * np.pi * rf[0]**3)
    densb[0] = 3 * Mbar[0] / (4 * np.pi * rf[0]**3)
    densfin[0] = 3 * Mfin[0] / (4 * np.pi * rf[0]**3)
    for m in range(1, len(rf)):
        densdm[m] = 3 * (Mdm[m] - Mdm[m-1]) / (4 * np.pi * (rf[m]**3 - rf[m
    -1]**3))
        densb[m] = 3 * (Mbar[m] - Mbar[m-1]) / (4 * np.pi * (rf[m]**3 - rf[m
    -1]**3))
        densfin[m] = 3 * (Mfin[m] - Mfin[m-1]) / (4 * np.pi * (rf[m]**3 - rf[m
    -1]**3))

    vdm, vbar, vfin = np.zeros(len(rf)), np.zeros(len(rf)), np.zeros(len(rf))
    for m in range(len(ri)):
        vdm[m] = (Mdm[m] * G / rf[m])**0.5
        vbar[m] = (Mbar[m] * G / rf[m])**0.5
        vfin[m] = (vdm[m]**2 + vbar[m]**2)**0.5

    axs[0][0].plot(rf, vfin*pc, '-.', label = 'f = %.2f' %f[j])
    axs[1][0].plot(rf, densfin*1e-1, '-.', label = 'f = %.2f' %f[j])

```

```
    if f[j] == 0.1:          # can be changed to 0.05 or 0.20 if necessary
        vbar2, vdm2 = vbar, vdm
        densb2, densdm2 = densb, densdm

        axs[0][0].plot(rf, vbar2*pc, 'k-', label = 'f = %.2f, baryons' %f[j])
        axs[0][0].plot(rf, vdm2*pc, 'k--', label = 'f = %.2f, dm only' %f[j])
        axs[1][0].plot(rf, densb2*1e-1, 'k-', label = 'f = %.2f, baryons' %f[j])
        axs[1][0].plot(rf, densdm2*1e-1, 'k--', label = 'f = %.2f, dm only' %f[j])

densinit = np.empty(len(ri))
densinit[0] = 3 * Minit[0] / (4 * np.pi * ri[0]**3)
for m in range(1, len(ri)):
    densinit[m] = 3 * (Minit[m] - Minit[m-1]) / (4 * np.pi * (ri[m]**3 - ri[m-1]**3))

vinit = np.zeros(len(ri))
for i in range(len(ri)):
    vinit[i] = (Minit[i] * G / ri[i])**0.5

axs[0][0].plot(ri, vinit*pc, 'k:', label = 'f = 0, initial curve')
axs[0][0].axvline(R_TF, 0, 1, color = 'k', linestyle = ':', linewidth = '0.7')
axs[0][0].grid(False)
axs[0][0].set_xlim(1e-2, 1e2), axs[0][0].set_ylim(5e-1, 400)
axs[0][0].set_xscale('log'), axs[0][0].set_yscale('log')
#axs[0][0].set_title('Rotation curves for scale length $b = %.2f$' %b)
axs[0][0].set_xlabel(r'$r$ [kpc]'), axs[0][0].set_ylabel(r'$v$ [km s$^{-1}$]')
axs[0][0].set_yticks([10, 20, 40, 60, 100, 200])
axs[0][0].set_yticklabels(['10', '20', '40', '60', '100', '200'])
#axs[0][0].text(0.05, 0.08, r'$10^{11}  M_\odot$', transform=axs[0][0].transAxes, fontsize=14)
axs[0][0].legend(loc='lower right', frameon=False)

axs2 = axs[0][0].twiny()
axs2.set_xlim(1e-2, 1e2)
axs2.set_xlabel('$r/R_{\mathrm{TF}}$')
axs2.set_xscale('log')

if R_TF == 0.1:
    axs2.set_xticks([0.1*R_TF, R_TF, 10*R_TF, 100*R_TF, 1000*R_TF])
    axs2.set_xticklabels(['0.1', '1', '10', '100', '1000'])
elif R_TF == 0.5:
    axs2.set_xticks([0.1*R_TF, R_TF, 10*R_TF, 100*R_TF])
    axs2.set_xticklabels(['0.1', '1', '10', '100'])
else:
    axs2.set_xticks([0.01*R_TF, 0.1*R_TF, 1*R_TF, 10*R_TF])
    axs2.set_xticklabels(['0.01','0.1', '1', '10'])

axs[1][0].plot(ri, densinit*1e-1, 'k:', label = 'f = 0, initial curve')
# dens*1e-1 for Mocz comparison
axs[1][0].axvline(R_TF, 0, 1, color = 'k', linestyle = ':', linewidth = '0.7')
#axs[1][0].set_title('Density curves for scale length $b = %.2f$' %b)
axs[1][0].set_xlabel(r'$\log r$ [kpc]'), axs[1][0].set_ylabel(r'$\log \rho$ [$10^{10} M_\odot$ kpc$^{-3}$]')
axs[1][0].set_xscale('log'), axs[1][0].set_yscale('log')
axs[1][0].set_xlim(1e-2, 1e2), axs[1][0].set_ylim(1e-7, 1e4)
#axs[1][0].legend(loc='best', frameon=False)

axs3 = axs[1][0].twiny()
axs3.set_xlim(1e-2, 1e2)
axs3.set_xlabel('$r/R_{\mathrm{TF}}$')
axs3.set_xscale('log')

```

```
178 if R_TF == 0.1:
179     axs3.set_xticks([0.1*R_TF, R_TF, 10*R_TF, 100*R_TF, 1000*R_TF])
180     axs3.set_xticklabels(['0.1', '1', '10', '100', '1000'])
181 elif R_TF == 0.5:
182     axs3.set_xticks([0.1*R_TF, R_TF, 10*R_TF, 100*R_TF])
183     axs3.set_xticklabels(['0.1', '1', '10', '100'])
184 else:
185     axs3.set_xticks([0.01*R_TF, 0.1*R_TF, R_TF, 10*R_TF])
186     axs3.set_xticklabels(['0.01','0.1', '1', '10'])
187 
188 plt.tight_layout()
```

Bibliography

L. Amendola and R. Barbieri. Dark matter from an ultra-light pseudo-Goldstone-boson. *Physics Letters B*, 642(3):192–196, Nov. 2006. doi: 10.1016/j.physletb.2006.08.069.

M. R. Baldeschi, G. B. Gelmini, and R. Ruffini. On massive fermions and bosons in galactic halos. *Physics Letters B*, 122(3-4):221–224, Mar. 1983. doi: 10.1016/0370-2693(83)90688-3.

J. Barnes and S. D. M. White. The response of a spheroid to a disc field or were bulges ever ellipticals? *Monthly Notices of the Royal Astronomical Society*, 211(4):753–765, 12 1984. ISSN 0035-8711. doi: 10.1093/mnras/211.4.753. URL `https://doi.org/10.1093/mnras/211.4.753`.

K. G. Begeman, A. H. Broeils, and R. H. Sanders. Extended rotation curves of spiral galaxies : dark haloes and modified dynamics. *Monthly Notices of the Royal Astronomical Society*, 249:523, Apr. 1991. doi: 10.1093/mnras/249.3.523.

G. Bertone and D. Hooper. History of dark matter. *Reviews of Modern Physics*, 90(4):045002, Oct. 2018. doi: 10.1103/RevModPhys.90.045002.

G. Bertone, D. Hooper, and J. Silk. Particle dark matter: evidence, candidates and constraints. *Physics Reports*, 405(5-6):279–390, Jan. 2005. doi: 10.1016/j.physrep.2004.08.031.

J. Binney and S. Tremaine. *Galactic Dynamics: Second Edition*. 2008.

D. Blas, J. Lesgourgues, and T. Tram. The Cosmic Linear Anisotropy Solving System (CLASS). Part II: Approximation schemes. *Journal of Cosmology and Astroparticle Physics*, 2011(7):034, July 2011. doi: 10.1088/1475-7516/2011/07/034.

G. R. Blumenthal, H. Pagels, and J. R. Primack. Galaxy formation by dissipationless particles heavier than neutrinos. *Nature*, 299(5878):37–38, Sept. 1982. doi: 10.1038/299037a0.

G. R. Blumenthal, S. M. Faber, R. Flores, and J. R. Primack. Contraction of dark matter galactic halos due to baryonic infall. *The Astrophysical Journal*, 301:27–34, Feb. 1986. doi: 10.1086/163867.

D. Boccaletti and G. Pucacco. *Theory of Orbits. Volume 1: Integrable Systems and Non-perturbative Methods*. Springer, 2004.

D. Bohm. A Suggested Interpretation of the Quantum Theory in Terms of "Hidden" Variables. I. *Physical Review*, 85(2):166–179, Jan. 1952. doi: 10.1103/PhysRev.85.166.

J. R. Bond, A. S. Szalay, and M. S. Turner. Formation of galaxies in a gravitino-dominated universe. *Physical Review Letters*, 48:1636–1639, Jun 1982. doi: 10.1103/PhysRevLett.48.1636. URL `https://link.aps.org/doi/10.1103/PhysRevLett.48.1636`.

J. Bovy. galpy: A python Library for Galactic Dynamics. *The Astrophysical Journal Supplement Series*, 216(2):29, Feb. 2015. doi: 10.1088/0067-0049/216/2/29.

M. Boylan-Kolchin, J. S. Bullock, and M. Kaplinghat. The Milky Way's bright satellites as an apparent failure of ΛCDM. *Monthly Notices of the Royal Astronomical Society*, 422(2):1203–1218, May 2012. doi: 10.1111/j.1365-2966.2012.20695.x.

J. S. Bullock and M. Boylan-Kolchin. Small-Scale Challenges to the ΛCDM Paradigm. *Annual Review of Astronomy and Astrophysics*, 55(1):343–387, Aug. 2017. doi: 10.1146/annurev-astro-091916-055313.

B. Carr and F. Kühnel. Primordial Black Holes as Dark Matter: Recent Developments. *Annual Review of Nuclear and Particle Science*, 70:355–394, Oct. 2020. doi: 10.1146/annurev-nucl-050520-125911.

M. Cautun, A. Benítez-Llambay, A. J. Deason, C. S. Frenk, A. Fattahi, F. A. Gómez, R. J. J. Grand, K. A. Oman, J. F. Navarro, and C. M. Simpson. The Milky Way total mass profile as inferred from Gaia DR2. *Monthly Notices of the Royal Astronomical Society*, 494(3):4291–4313, May 2020. doi: 10.1093/mnras/staa1017.

P.-H. Chavanis. Predictive model of BEC dark matter halos with a solitonic core and an isothermal atmosphere. *Physical Review D*, 100(8), Oct 2019. ISSN 2470-0029. doi: 10.1103/physrevd.100.083022. URL `http://dx.doi.org/10.1103/PhysRevD.100.083022`.

P.-H. Chavanis. Derivation of the core mass-halo mass relation of fermionic and bosonic dark matter halos from an effective thermodynamical model. *Physical Review D*, 100(12):123506, Dec. 2019. doi: 10.1103/PhysRevD.100.123506.

T. Dawoodbhoy, P. R. Shapiro, and T. Rindler-Daller. Core-envelope haloes in scalar field dark matter with repulsive self-interaction: fluid dynamics beyond the de Broglie wavelength. *Monthly Notices of the Royal Astronomical Society*, 506(2):2418–2444, Sept. 2021. doi: 10.1093/mnras/stab1859.

W. J. G. de Blok. The Core-Cusp Problem. *Advances in Astronomy*, 2010: 789293, Jan. 2010. doi: 10.1155/2010/789293.

DES Collaboration. Dark Energy Survey Year 3 results: Curved-sky weak lensing mass map reconstruction. *Monthly Notices of the Royal Astronomical Society*, 505(3):4626–4645, Aug. 2021. doi: 10.1093/mnras/stab1495.

A. R. Duffy, J. Schaye, S. T. Kay, C. Dalla Vecchia, R. A. Battye, and C. M. Booth. Impact of baryon physics on dark matter structures: a detailed simulation study of halo density profiles. *Monthly Notices of the Royal Astronomical Society*, 405(4):2161–2178, July 2010. doi: 10.1111/j.1365-2966.2010.16613.x.

F. W. Dyson, A. S. Eddington, and C. Davidson. A Determination of the Deflection of Light by the Sun's Gravitational Field, from Observations Made at the Total Eclipse of May 29, 1919. *Philosophical Transactions of the Royal Society of London Series A*, 220:291–333, Jan. 1920. doi: 10.1098/rsta.1920.0009.

D. Egana-Ugrinovic, R. Essig, D. Gift, and M. LoVerde. The cosmological evolution of self-interacting dark matter. *Journal of Cosmology and Astroparticle Physics*, 2021(5):013, May 2021. doi: 10.1088/1475-7516/2021/05/013.

O. J. Eggen, D. Lynden-Bell, and A. R. Sandage. Evidence from the motions of old stars that the Galaxy collapsed. *The Astrophysical Journal*, 136:748, Nov. 1962. doi: 10.1086/147433.

A. Einstein. Zur Elektrodynamik bewegter Körper. *Annalen der Physik*, 322 (10):891–921, Jan. 1905. doi: 10.1002/andp.19053221004.

A. Einstein. Die Grundlage der allgemeinen Relativitätstheorie. *Annalen der Physik*, 354(7):769–822, Jan. 1916. doi: 10.1002/andp.19163540702.

J. Ellis, J. S. Hagelin, D. V. Nanopoulos, K. Olive, and M. Srednicki. Supersymmetric relics from the Big Bang. *Nuclear Physics B*, 238(2):453–476, June 1984. doi: 10.1016/0550-3213(84)90461-9.

B. Famaey and J. Binney. Modified Newtonian dynamics in the Milky Way. *Monthly Notices of the Royal Astronomical Society*, 363(2):603–608, Oct. 2005. doi: 10.1111/j.1365-2966.2005.09474.x.

D. J. Fixsen. The Temperature of the Cosmic Microwave Background. *The Astrophysical Journal*, 707(2):916–920, Dec. 2009. doi: 10.1088/0004-637X/707/2/916.

P. H. Frampton. Searching for dark matter constituents with many solar masses. *Modern Physics Letters A*, 31(16):1650093, May 2016. doi: 10.1142/S0217732316500930.

K. Freese, P. Gondolo, J. A. Sellwood, and D. Spolyar. Dark Matter Densities During the Formation of the First Stars and in Dark Stars. *The Astrophysical Journal*, 693(2):1563–1569, Mar. 2009. doi: 10.1088/0004-637X/693/2/1563.

O. Y. Gnedin, A. V. Kravtsov, A. A. Klypin, and D. Nagai. Response of dark matter halos to condensation of baryons: Cosmological simulations and improved adiabatic contraction model. *The Astrophysical Journal*, 616 (1):16–26, Nov 2004. ISSN 1538-4357. doi: 10.1086/424914. URL `http://dx.doi.org/10.1086/424914`.

H. Goldberg. Constraint on the Photino Mass from Cosmology. *Physical Review Letters*, 50(19):1419–1422, May 1983. doi: 10.1103/PhysRevLett.50.1419.

H. Goldstein, C. Poole, and J. Safko. *Classical Mechanics (3rd Edition)*. Addison-Wesley, 2001.

D. T. Greenwood. *Classical Dynamics*. Courier Corporation, 1997.

E. P. Gross. Structure of a quantized vortex in boson systems. *Il Nuovo Cimento*, 20(3):454–477, May 1961. doi: 10.1007/BF02731494.

S. W. Hawking. Black holes from cosmic strings. *Physics Letters B*, 231(3): 237–239, Nov. 1989. doi: 10.1016/0370-2693(89)90206-2.

M. Henon. L'amas isochrone: I. *Annales d'Astrophysique*, 22:126, Feb. 1959a.

M. Henon. II. Le calcul des orbites. *Annales d'Astrophysique*, 22:491, Feb. 1959b.

L. Hernquist. An Analytical Model for Spherical Galaxies and Bulges. *The Astrophysical Journal*, 356:359, June 1990. doi: 10.1086/168845.

S. Hossenfelder and T. Mistele. Strong lensing with superfluid dark matter. *Journal of Cosmology and Astroparticle Physics*, 2019(2):001, Feb. 2019. doi: 10.1088/1475-7516/2019/02/001.

W. Hu, R. Barkana, and A. Gruzinov. Fuzzy Cold Dark Matter: The Wave Properties of Ultralight Particles. *Physical Review Letters*, 85(6):1158–1161, Aug. 2000. doi: 10.1103/PhysRevLett.85.1158.

E. Hubble. A Relation between Distance and Radial Velocity among Extra-Galactic Nebulae. *Proceedings of the National Academy of Science*, 15(3): 168–173, Mar. 1929. doi: 10.1073/pnas.15.3.168.

L. Hui, J. P. Ostriker, S. Tremaine, and E. Witten. Ultralight scalars as cosmological dark matter. *Physical Review D*, 95(4):043541, Feb. 2017. doi: 10.1103/PhysRevD.95.043541.

G. Jungman, M. Kamionkowski, and K. Griest. Supersymmetric dark matter. *Physics Reports*, 267:195–373, Mar. 1996. doi: 10.1016/0370-1573(95)00058-5.

M. Kaplinghat, M. Valli, and H.-B. Yu. Too big to fail in light of Gaia. *Monthly Notices of the Royal Astronomical Society*, 490(1):231–242, Nov. 2019. doi: 10.1093/mnras/stz2511.

J. C. Kapteyn. First Attempt at a Theory of the Arrangement and Motion of the Sidereal System. *The Astrophysical Journal*, 55:302, May 1922. doi: 10.1086/142670.

A. Klypin, A. V. Kravtsov, O. Valenzuela, and F. Prada. Where Are the Missing Galactic Satellites? *The Astrophysical Journal*, 522(1):82–92, Sept. 1999. doi: 10.1086/307643.

A. Klypin, G. Yepes, S. Gottlöber, F. Prada, and S. Heß. MultiDark simulations: the story of dark matter halo concentrations and density profiles. *Monthly Notices of the Royal Astronomical Society*, 457(4):4340–4359, Apr. 2016. doi: 10.1093/mnras/stw248.

J. Lesgourgues. The Cosmic Linear Anisotropy Solving System (CLASS) I: Overview. *arXiv e-prints*, art. arXiv:1104.2932, Apr. 2011.

B. Li, T. Rindler-Daller, and P. R. Shapiro. Cosmological constraints on Bose-Einstein-condensed scalar field dark matter. *Physical Review D*, 89 (8), Apr 2014. ISSN 1550-2368. doi: 10.1103/physrevd.89.083536. URL `http://dx.doi.org/10.1103/PhysRevD.89.083536`.

B. Li, P. R. Shapiro, and T. Rindler-Daller. Bose-Einstein-condensed scalar field dark matter and the gravitational wave background from inflation: New cosmological constraints and its detectability by LIGO. , 96(6):063505, Sept. 2017. doi: 10.1103/PhysRevD.96.063505.

E. Madelung. Quantentheorie in hydrodynamischer Form. *Zeitschrift für Physik*, 40(3-4):322–326, Mar. 1927. doi: 10.1007/BF01400372.

J. Magaña and T. Matos. A brief Review of the Scalar Field Dark Matter model. In *Journal of Physics Conference Series*, volume 378 of *Journal of Physics Conference Series*, page 012012, Aug. 2012. doi: 10.1088/1742-6596/378/1/012012.

M. Milgrom. A modification of the Newtonian dynamics as a possible alternative to the hidden mass hypothesis. *The Astrophysical Journal*, 270:365–370, July 1983. doi: 10.1086/161130.

P. Mocz, M. Vogelsberger, V. H. Robles, J. Zavala, M. Boylan-Kolchin, A. Fialkov, and L. Hernquist. Galaxy formation with BECDM - I. Turbulence and relaxation of idealized haloes. *Monthly Notices of the Royal Astronomical Society*, 471(4):4559–4570, Nov. 2017. doi: 10.1093/mnras/stx1887.

P. Mocz, A. Fialkov, M. Vogelsberger, F. Becerra, X. Shen, V. H. Robles, M. A. Amin, J. Zavala, M. Boylan-Kolchin, S. Bose, F. Marinacci, P.-H. Chavanis,

L. Lancaster, and L. Hernquist. Galaxy formation with BECDM - II. Cosmic filaments and first galaxies. *Monthly Notices of the Royal Astronomical Society*, 494(2):2027–2044, May 2020. doi: 10.1093/mnras/staa738.

J. F. Navarro, C. S. Frenk, and S. D. M. White. The Structure of Cold Dark Matter Halos. *The Astrophysical Journal*, 462:563, May 1996. doi: 10.1086/177173.

R. D. Peccei. *The Strong CP Problem and Axions*, volume 741, page 3. 2008.

R. D. Peccei and H. R. Quinn. CP conservation in the presence of pseudoparticles. *Physical Review Letters*, 38(25):1440–1443, June 1977. doi: 10.1103/PhysRevLett.38.1440.

P. J. E. Peebles. Large-scale background temperature and mass fluctuations due to scale-invariant primeval perturbations. *The Astrophysical Journal Letters*, 263:L1–L5, Dec. 1982. doi: 10.1086/183911.

A. A. Penzias and R. W. Wilson. A Measurement of Excess Antenna Temperature at 4080 Mc/s. *The Astrophysical Journal*, 142:419–421, July 1965. doi: 10.1086/148307.

L. P. Pitaevskii. Vortex lines in an imperfect bose gas. *Sov. Phys.-JETP*, 13 (2):451, 1961. URL `https://ci.nii.ac.jp/naid/10011892708/en/`.

L. P. Pitaevskii and S. Stringari. *Bose-Einstein condensation*. Oxford University Press, 2003.

Planck Collaboration. Planck 2018 results. VI. Cosmological parameters. *Astronomy and Astrophysics*, 641:A6, Sept. 2020. doi: 10.1051/0004-6361/201833910.

H. Poincaré. The Milky Way and the Theory of Gases. *Popular Astronomy*, 14:475–488, Oct. 1906.

A. M. Price-Whelan. Gala: A python package for galactic dynamics. *The Journal of Open Source Software*, 2(18), Oct. 2017. doi: 10.21105/joss.00388. URL `https://doi.org/10.21105%2Fjoss.00388`.

T. Rindler-Daller. Understanding CMB physics through the exploration of exotic cosmological models: a classroom study using CLASS. *European Journal of Physics*, 41(3):035602, May 2020. doi: 10.1088/1361-6404/ab6c6b.

T. Rindler-Daller and P. R. Shapiro. Angular momentum and vortex formation in Bose-Einstein-condensed cold dark matter haloes. *Monthly Notices of the Royal Astronomical Society*, 422(1):135–161, May 2012. doi: 10.1111/j.1365-2966.2012.20588.x.

M. S. Roberts and A. H. Rots. Comparison of Rotation Curves of Different Galaxy Types. *Astronomy and Astrophysics*, 26:483–485, Aug. 1973.

V. H. Robles and T. Matos. Exact Solution to Finite Temperature SFDM: Natural Cores without Feedback. *The Astrophysical Journal*, 763(1):19, Jan. 2013. doi: 10.1088/0004-637X/763/1/19.

V. H. Robles, J. S. Bullock, and M. Boylan-Kolchin. Scalar field dark matter: helping or hurting small-scale problems in cosmology? *Monthly Notices of the Royal Astronomical Society*, 483(1):289–298, Feb. 2019. doi: 10.1093/mnras/sty3190.

D. H. Rogstad and G. S. Shostak. Gross Properties of Five Scd Galaxies as Determined from 21-centimeter Observations. *The Astrophysical Journal*, 176:315, Sept. 1972. doi: 10.1086/151636.

V. C. Rubin and J. Ford, W. Kent. Rotation of the Andromeda Nebula from a Spectroscopic Survey of Emission Regions. *The Astrophysical Journal*, 159: 379, Feb. 1970. doi: 10.1086/150317.

B. S. Ryden and J. E. Gunn. Galaxy Formation by Gravitational Collapse. *The Astrophysical Journal*, 318:15, July 1987. doi: 10.1086/165349.

J. L. Sanders and J. Binney. Actions, angles and frequencies for numerically integrated orbits. *Monthly Notices of the Royal Astronomical Society*, 441(4): 3284–3295, July 2014. doi: 10.1093/mnras/stu796.

H.-Y. Schive, M.-H. Liao, T.-P. Woo, S.-K. Wong, T. Chiueh, T. Broadhurst, and W. Y. P. Hwang. Understanding the Core-Halo Relation of Quantum Wave Dark Matter from 3D Simulations. *Physical Review Letters*, 113(26): 261302, Dec. 2014. doi: 10.1103/PhysRevLett.113.261302.

H.-Y. Schive, T. Chiueh, T. Broadhurst, and K.-W. Huang. Contrasting Galaxy Formation from Quantum Wave Dark Matter, ψDM, with ΛCDM, using Planck and Hubble Data. *The Astrophysical Journal*, 818(1):89, Feb. 2016. doi: 10.3847/0004-637X/818/1/89.

S. O. Schobesberger, T. Rindler-Daller, and P. R. Shapiro. Angular momentum and the absence of vortices in the cores of fuzzy dark matter haloes. *Monthly Notices of the Royal Astronomical Society*, 505(1):802–829, July 2021. doi: 10.1093/mnras/stab1153.

B. Schwabe, J. C. Niemeyer, and J. F. Engels. Simulations of solitonic core mergers in ultralight axion dark matter cosmologies. *Physical Review D*, 94 (4):043513, Aug. 2016. doi: 10.1103/PhysRevD.94.043513.

S. F. Shandarin, A. G. Doroshkevich, and Y. B. Zel'dovich. The large-scale structure of the universe. *Uspekhi Fizicheskikh Nauk*, 139:83–134, Jan. 1983.

P. R. Shapiro, T. Dawoodbhoy, and T. Rindler-Daller. Cosmological structure formation in scalar field dark matter with repulsive self-interaction: The Incredible Shrinking Jeans Mass. *arXiv e-prints*, art. arXiv:2106.13244, June 2021.

D. N. Spergel and P. J. Steinhardt. Observational Evidence for Self-Interacting Cold Dark Matter. *Physical Review Letters*, 84(17):3760–3763, Apr. 2000. doi: 10.1103/PhysRevLett.84.3760.

P. Stäckel. Über die Integration der Hamilton-Jacobischen Differentialgleichung mittelst Separation der Variabeln, 1891. Habilitationsschrift.

T. Treu. Strong Lensing by Galaxies. *Annual Review of Astronomy and Astrophysics*, 48:87–125, Sept. 2010. doi: 10.1146/annurev-astro-081309-130924.

P. van Dokkum, S. Danieli, Y. Cohen, A. Merritt, A. J. Romanowsky, R. Abraham, J. Brodie, C. Conroy, D. Lokhorst, L. Mowla, E. O'Sullivan, and J. Zhang. A galaxy lacking dark matter. *Nature*, 555(7698):629–632, Mar. 2018. doi: 10.1038/nature25767.

D. H. Weinberg, J. S. Bullock, F. Governato, R. Kuzio de Naray, and A. H. G. Peter. Cold dark matter: Controversies on small scales. *Proceedings of the National Academy of Science*, 112(40):12249–12255, Oct. 2015. doi: 10.1073/pnas.1308716112.

S. Weinberg. A new light boson? *Physical Review Letters*, 40(4):223–226, Jan. 1978. doi: 10.1103/PhysRevLett.40.223.

F. Wilczek. Problem of strong P and T invariance in the presence of instantons. *Physical Review Letters*, 40(5):279–282, Jan. 1978. doi: 10.1103/PhysRevLett.40.279.

R. E. Wyatt. *Quantum Dynamics with Trajectories - Introduction to Quantum Hydrodynamics*. Springer, 2005.

Y. B. Zel'dovich and I. D. Novikov. The Hypothesis of Cores Retarded during Expansion and the Hot Cosmological Model. *Soviet Astronomy*, 10:602, Feb. 1967.

Y. B. Zel'dovich, A. A. Klypin, M. Y. Khlopov, and V. M. Chechetkin. Astrophysical bounds on the mass of heavy stable neutral leptons. *Soviet Journal of Nuclear Physics*, 31:5, May 1980.

Y. B. Zel'dovich, J. Einasto, and S. F. Shandarin. Giant voids in the Universe. *Nature*, 300(5891):407–413, Dec. 1982. doi: 10.1038/300407a0.

F. Zwicky. Die Rotverschiebung von extragalaktischen Nebeln. *Helvetica Physica Acta*, 6:110–127, Jan. 1933.

List of Figures